

Fluid reservoir in the Hyuga-nada accretionary prism near the Kyushu-Palau ridge: insights from a passive seismic array

Takeshi Akuhara¹, Yusuke Yamashita², Shukei Ohyanagi², Yasunori Sawaki², Tomoaki Yamada³, and Masanao Shinohara³

¹Earthquake Research Institute, The University of Tokyo

²Kyoto University

³University of Tokyo

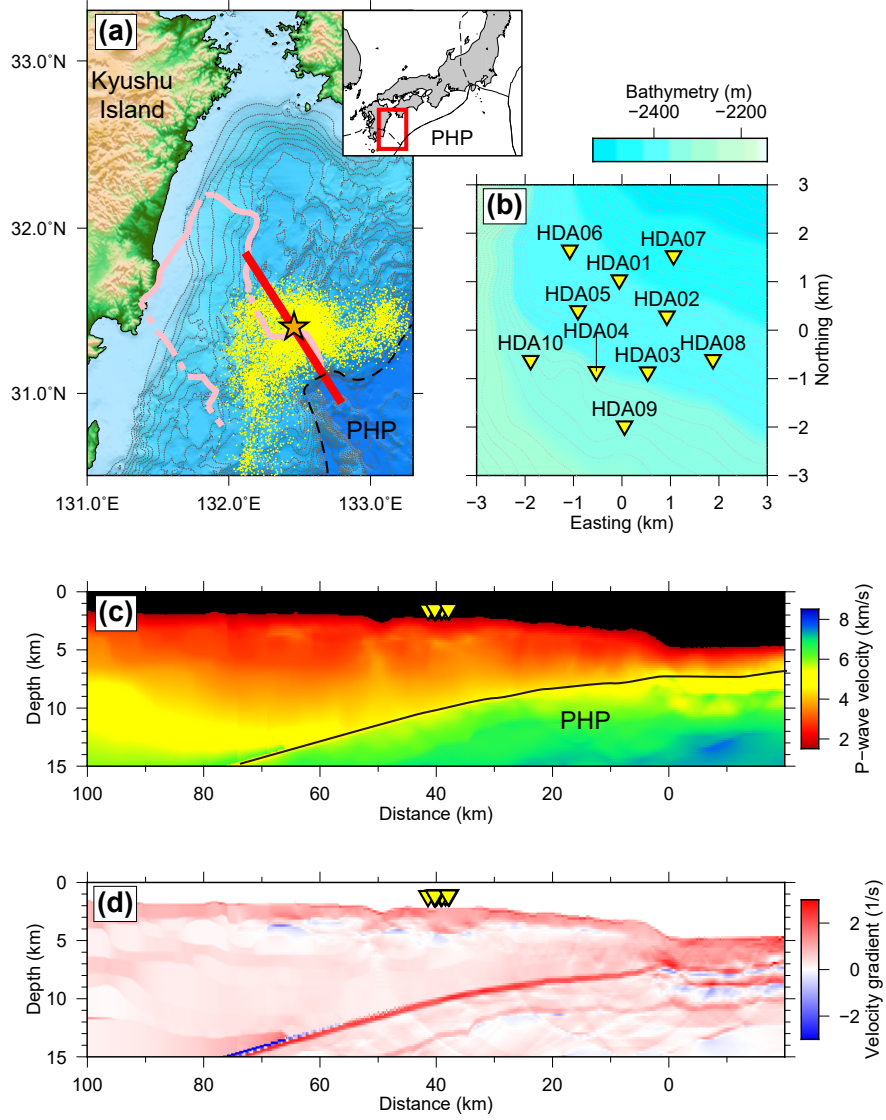
January 17, 2023

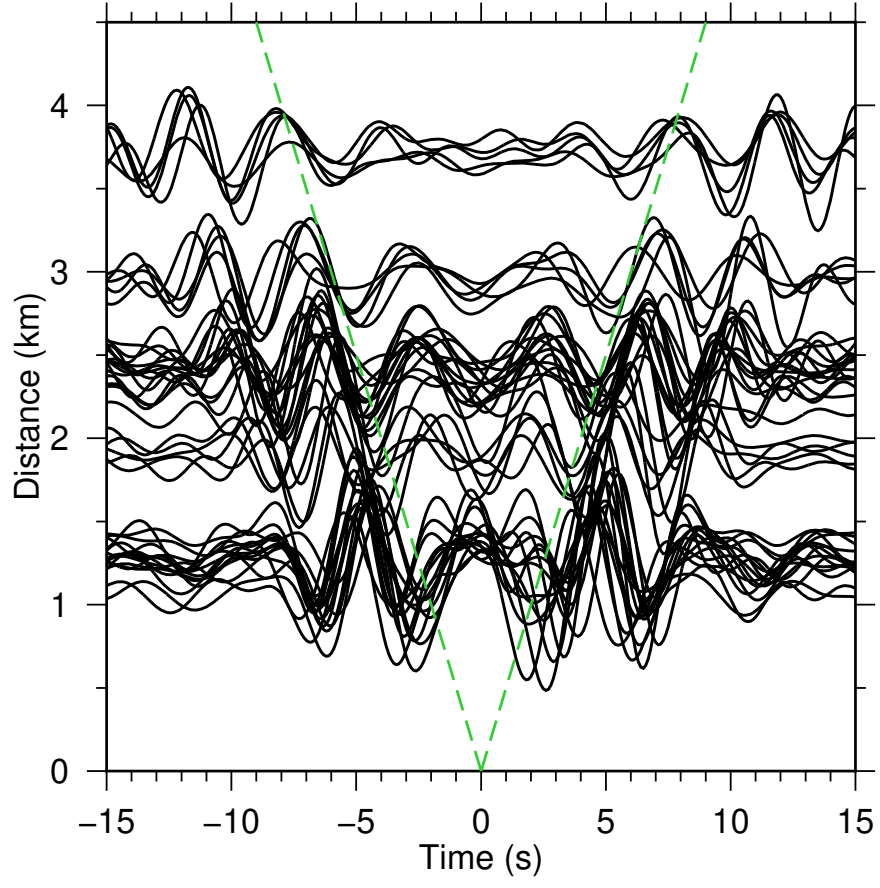
Abstract

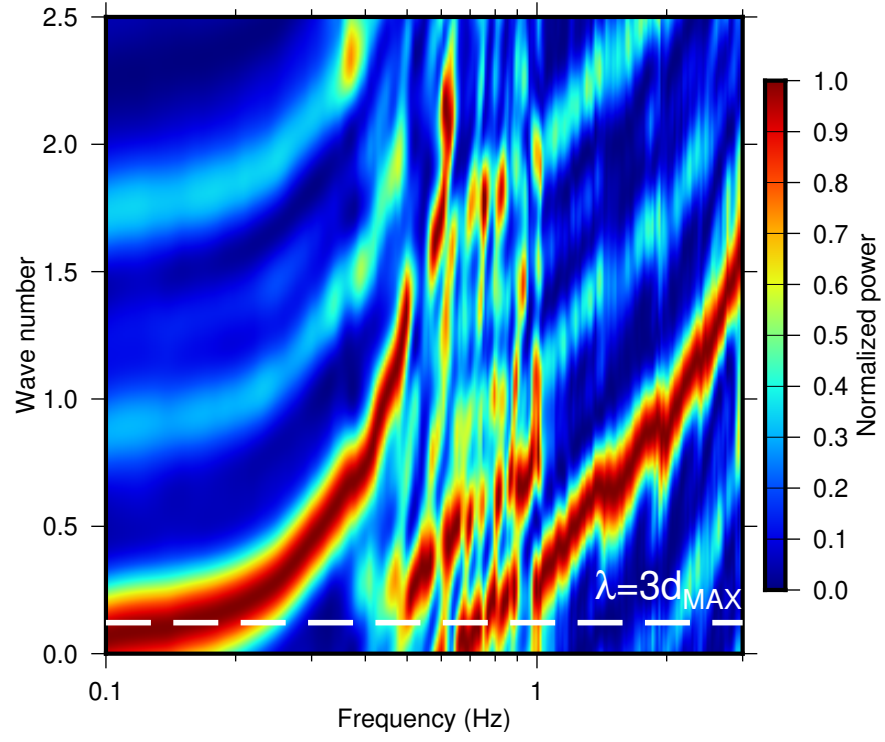
Shear wave velocity (V_s) estimations of accretionary prisms can pose unique constraints to the physical properties of rocks, which are hard to obtain from compressional velocities (V_p) alone. Thus, it would help better understand the fluid processes of the accretion system. This study investigates the V_s structure of the Hyuga-nada accretionary prism using an array of ocean-bottom seismometers (OBSs) with a 2 km radius. Teleseismic Green's functions and a surface wave dispersion curve are inverted to one-dimensional V_s structures using transdimensional inversion. The results indicate the presence of a low-velocity zone 3–4 km below the seafloor. The reduced V_s is consistent with a reduced V_p feature obtained in a previous seismic refraction survey. From its high V_p/V_s ratio, we conclude that the low velocities represent high pore fluid pressure. In addition, the resolved lithological boundary exhibits a sharp offset that extends laterally across the OBS array. We attribute this offset to a blind fault below while acknowledging other possibilities, such as due to mud diapirism. The predicted fault is located at the Kyushu–Palau Ridge flank, oriented roughly parallel to the ridge axis, and thus likely caused by ridge subduction. The fracture caused by the ridge subduction may act as a fluid conduit, forming a fluid reservoir beneath the well-compacted sediment layers.

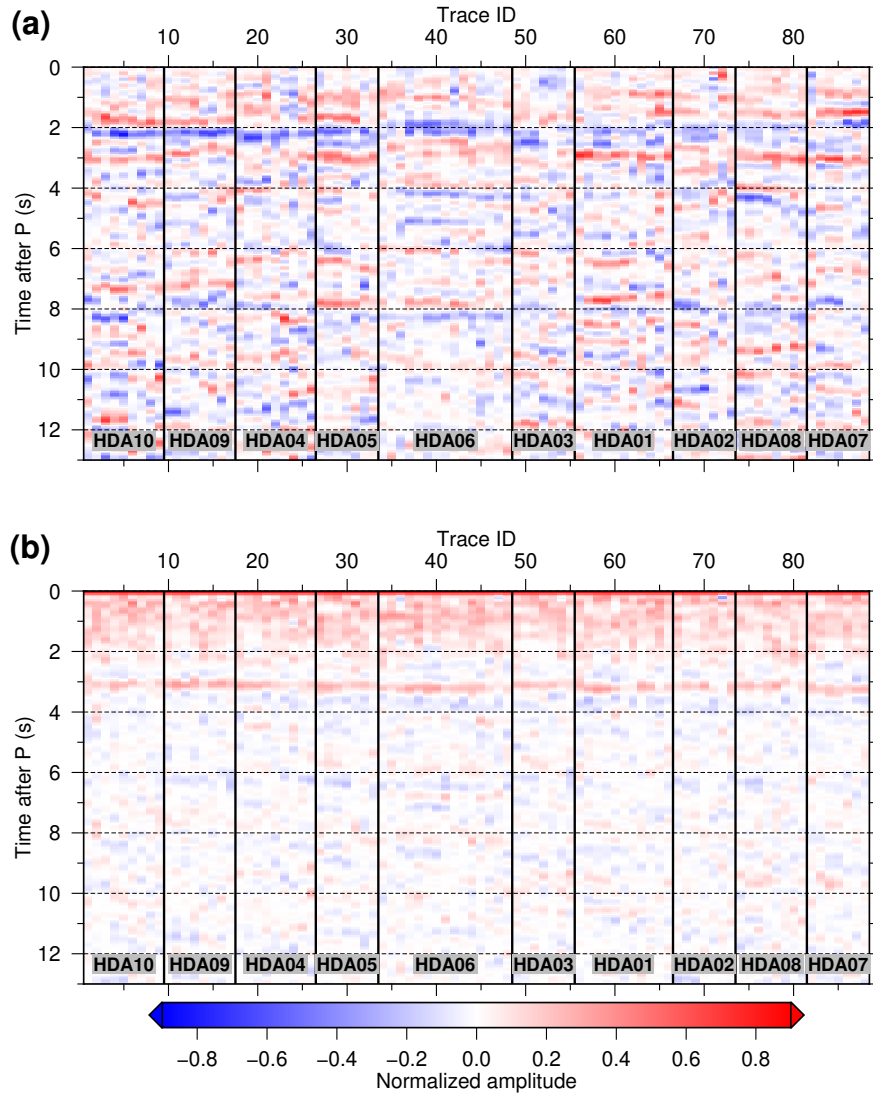
Hosted file

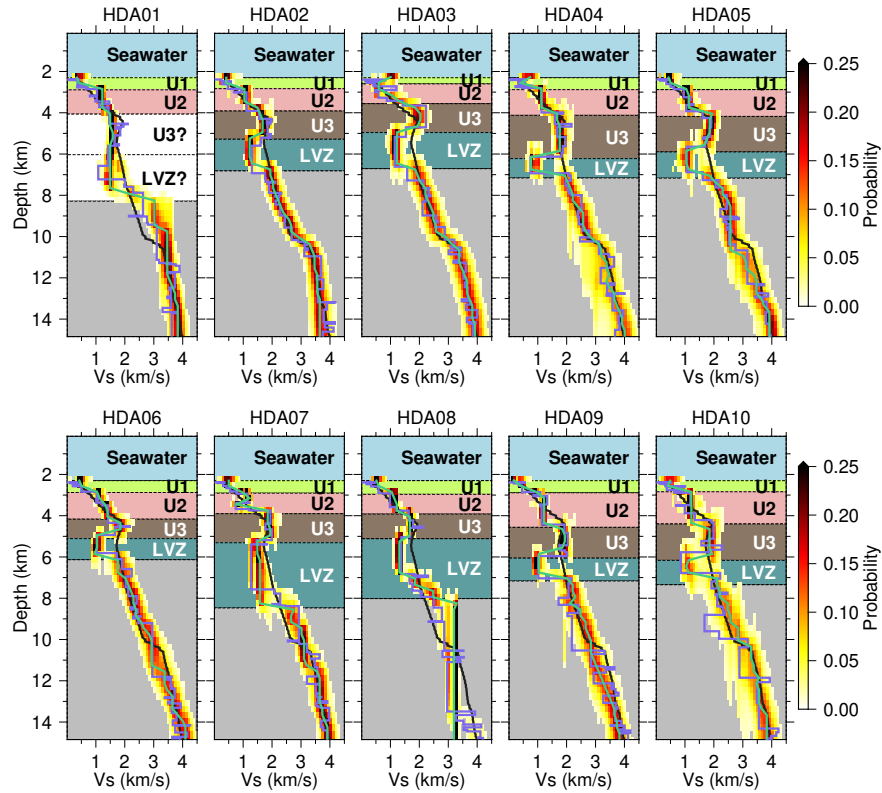
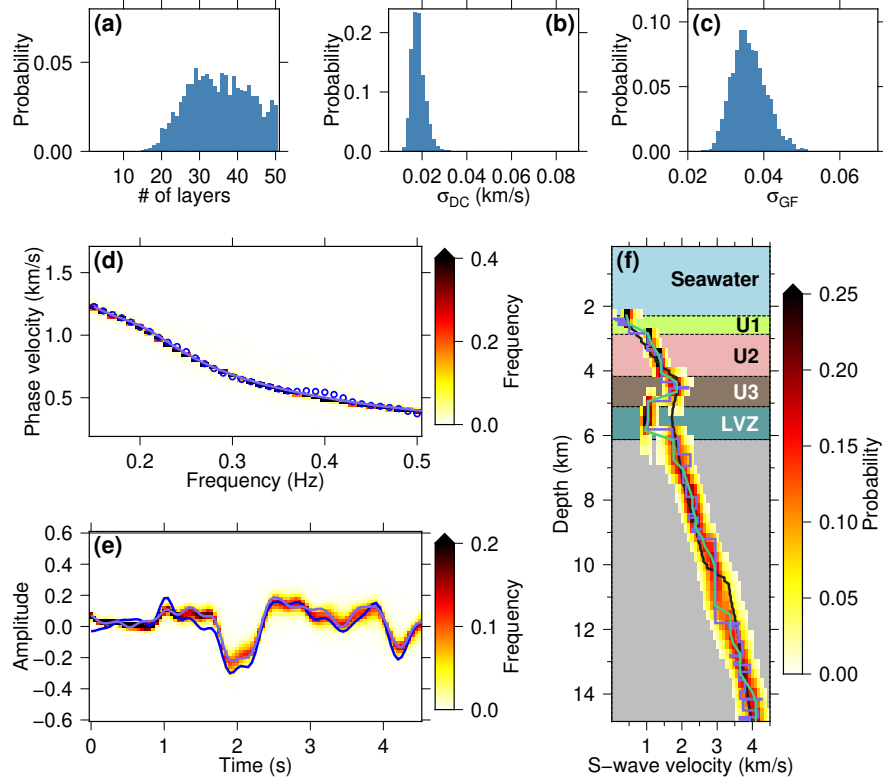
952491_0_art_file_10548950_rn63sr.docx available at <https://authorea.com/users/32145/articles/615355-fluid-reservoir-in-the-hyuga-nada-accretionary-prism-near-the-kyushu-palau-ridge-insights-from-a-passive-seismic-array>

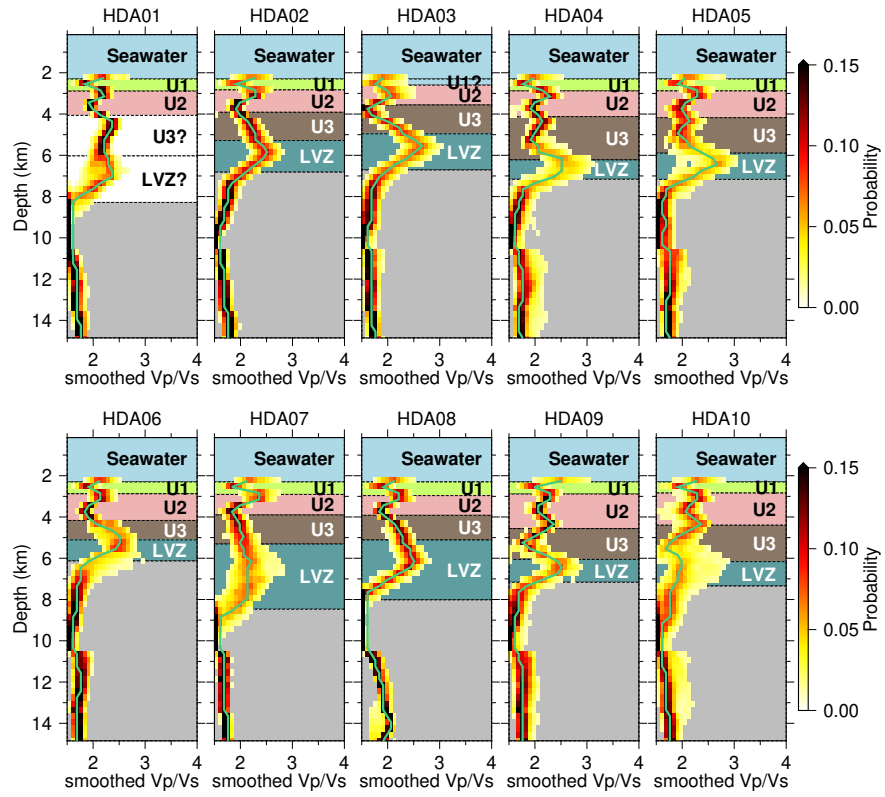


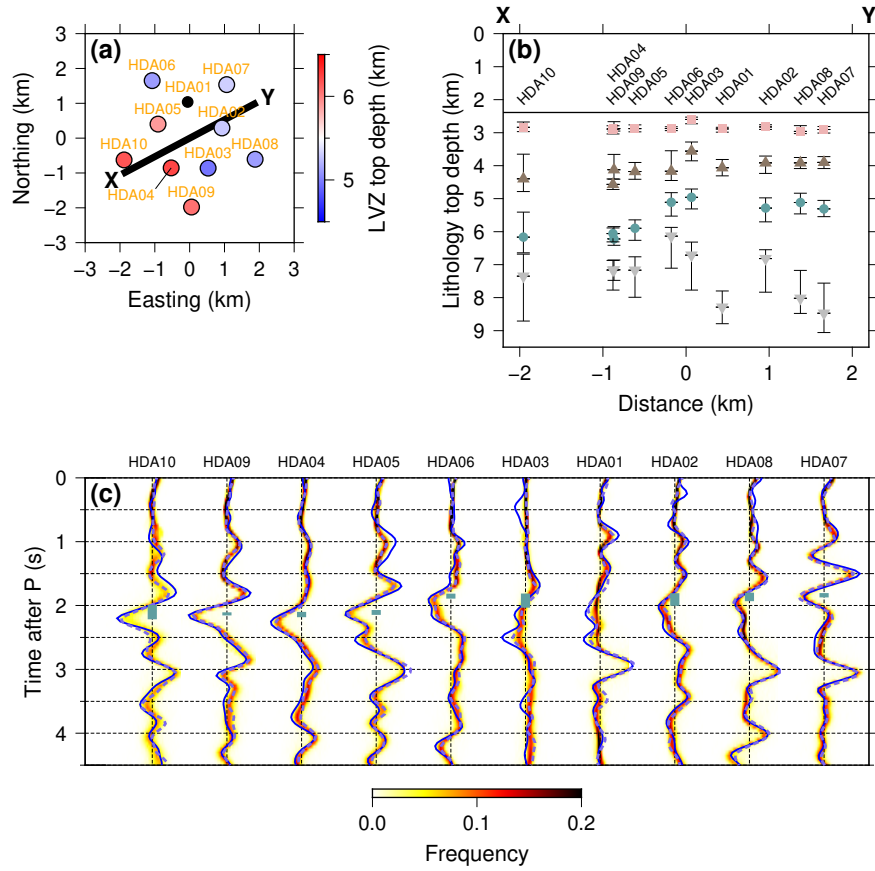


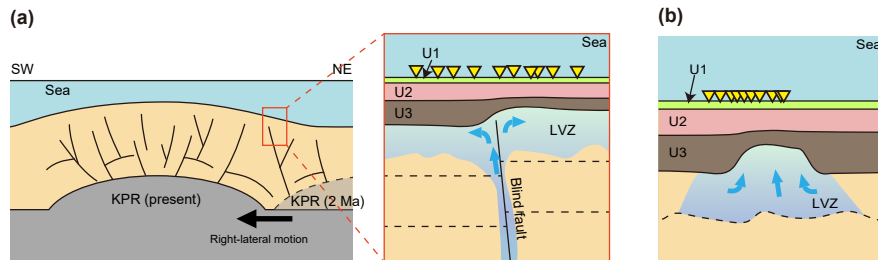
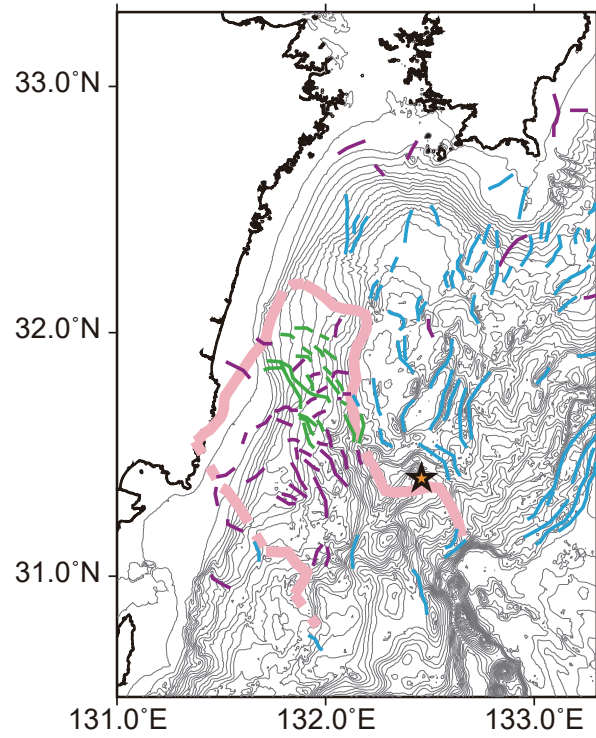












Hosted file

952491_0_supp_10548973_rn621w.docx available at <https://authorea.com/users/32145/articles/615355-fluid-reservoir-in-the-hyuga-nada-accretionary-prism-near-the-kyushu-palau-ridge-insights-from-a-passive-seismic-array>

1 **Fluid reservoir in the Hyuga-nada accretionary prism near the Kyushu-Palau**
2 **ridge: insights from a passive seismic array**

3 ¹Takeshi Akuhara

4 ²Yusuke Yamashita

5 ³Shukei Ohyanagi

6 ³Yasunori Sawaki

7 ¹Tomoaki Yamada

8 ¹Masanao Shinohara

9

10 ¹Earthquake Research Institute, The University of Tokyo, Tokyo, Japan

11 ²Disaster Prevention Research Institute, Kyoto University, Kyoto, Japan

12 ³Graduate School of Science, Kyoto University, Kyoto, Japan

13

14 Corresponding author:

15 Takeshi Akuhara (akuhara@eri.u-tokyo.ac.jp)

16

17 **Key points**

- 18 ● The shear wave velocity structures of the shallow Hyuga-nada accretionary prism
19 were derived using a passive seismic array.
- 20 ● A low shear velocity zone exists ~3–4 km below the seafloor, possibly indicative of
21 a fluid reservoir.
- 22 ● A Fault induced by the subducting Kyushu–Palau Ridge may act as a fluid pathway,
23 supplying fluids to the reservoir.

24

25 **Abstract**

26 Shear wave velocity (V_s) estimations of accretionary prisms can pose unique constraints
27 to the physical properties of rocks, which are hard to obtain from compressional
28 velocities (V_p) alone. Thus, it would help better understand the fluid processes of the
29 accretion system. This study investigates the V_s structure of the Hyuga-nada
30 accretionary prism using an array of ocean-bottom seismometers (OBSs) with a 2 km
31 radius. Teleseismic Green's functions and a surface wave dispersion curve are inverted
32 to one-dimensional V_s structures using transdimensional inversion. The results indicate
33 the presence of a low-velocity zone 3–4 km below the seafloor. The reduced V_s is
34 consistent with a reduced V_p feature obtained in a previous seismic refraction survey.
35 From its high V_p/V_s ratio, we conclude that the low velocities represent high pore fluid
36 pressure. In addition, the resolved lithological boundary exhibits a sharp offset that
37 extends laterally across the OBS array. We attribute this offset to a blind fault below
38 while acknowledging other possibilities, such as due to mud diapirism. The predicted
39 fault is located at the Kyushu–Palau Ridge flank, oriented roughly parallel to the ridge
40 axis, and thus likely caused by ridge subduction. The fracture caused by the ridge
41 subduction may act as a fluid conduit, forming a fluid reservoir beneath the
42 well-compacted sediment layers.

43

44 **Plain language summary**

45 Propagation speeds of seismic S-waves offer unique constraints on physical properties
46 in shallow subduction zones, which is hard to know from only seismic P-wave velocity.
47 This study investigates the subsurface structure in Hyuga-nada in the southwestern
48 Japan subduction zone by exploring S-wave speeds. For this purpose, we use natural
49 seismic and noise data recorded by densely installed ocean-bottom seismometers. The
50 results reveal a region with a reduced S-wave velocity at a depth of ~3–4 km below the
51 seafloor, which may be a water reservoir. The depth of the potential water reservoir
52 changes abruptly across the array. This offset may suggest the presence of a hidden fault

53 below, although we cannot exclude other possibilities. We propose that a fault created
54 by subducting seamounts acts as a conduit that transports water to the reservoir.

55

56 **Keywords**

57 Hyuga-nada

58 Kyushu–Palau Ridge

59 Fluid reservoir

60 Transdimensional inversion

61 Ocean-bottom seismometer

62

63

64 **1. Introduction**

65 Fluids, which may influence the slip behaviors of faults by increasing pore
66 pressure, are crucial for understanding the subduction–accretion system. They have
67 been associated with the seismic cycle (Van Dinther et al., 2013), the genesis of slow
68 earthquakes (Saffer & Wallace, 2015), and wedge development (Wang & Hu, 2006).
69 Recent studies have shown that subducted reliefs such as seamounts and ridges play a
70 critical role in hydrology. Seamounts reportedly induce fractures within the overriding
71 plate, which increases permeability (Chesley et al., 2021; Sahling et al., 2008; Sun et al.,
72 2020). High-resolution P-wave velocity (V_p) structures provided by active-source
73 seismic surveys have illuminated fluid distribution in accretionary prisms. Still,
74 additional constraints from S-wave velocity (V_s) are essential to gain further insights
75 into subsurface rock properties, especially the pore fluid pressure (Akuhara et al., 2020;
76 Arnulf et al., 2021; Tsuji et al., 2011).

77 Hyuga-nada, located in the westernmost southwestern Japan subduction zone, is a
78 region facing ridge subduction (**Figure 1**). The incoming Philippine Sea Plate hosts the
79 Kyushu–Palau Ridge (KPR) with a NNW–SSE strike. The subducted portion of this
80 ridge has been identified by seismological studies employing either passive or active
81 seismic sources (Park et al., 2009; Yamamoto et al., 2013). The subduction of the KPR
82 beneath the Kyushu started at 5 Ma; the convergence direction was almost parallel to
83 the ridge axis and perpendicular to the trench (Mahony et al., 2011). At 1–2 Ma, the
84 subduction direction slightly rotated counterclockwise; consequently, the subduction
85 accompanies the right-lateral motion (Itoh et al., 1998; Yamazaki & Okamura, 1989).
86 Tectonic tremors and very-low-frequency earthquakes, both are members of slow
87 earthquakes, intermittently occur near the KPR with an interval of 1–3 years (Baba et al.,
88 2020; Tonegawa et al., 2020; Yamashita et al., 2015, 2021). As suggested for other

89 regions worldwide, these slow earthquake activities may reflect a fluid-rich
90 environment near the plate interface (Saffer & Wallace, 2015). However, little is known
91 about the fluid processes (e.g., fluid sources, pathways, reservoirs) in this region.

92 High-resolution structures of the accretionary prism in this region were obtained
93 in previous active-source seismic surveys (Nakanishi et al., 2018; Nishizawa et al.,
94 2009; Park et al., 2009). **Figure 1c** shows a P-wave velocity (V_p) model based on a
95 refraction survey (Nakanishi et al., 2018). Overall, the accretionary prism shows V_p of
96 2–4 km/s, and the subducting Philippine Sea Plate has a higher velocity of >6 km/s
97 beneath the prism. Interestingly, velocity inversion with depth is noticeable at ~2 km
98 beneath the seafloor (**Figure 1d**). Nishizawa et al. (2009) reported a similar low-velocity
99 zone (LVZ) beneath another independent seismic profile in Hyuga-nada. These LVZs
100 may indicate fluid-rich conditions, although previous studies have not provided a
101 detailed interpretation. The challenges are the modest sensitivity of the refraction
102 surveys to thin LVZs with a sharp velocity contrast and the interpretation of physical
103 properties based on V_p alone.

104 This study investigates the shear wave velocity (V_s) structure by utilizing a dense
105 passive seismic array of ocean-bottom seismometers (OBSs) deployed in the
106 Hyuga-nada region. Traditionally, active-source seismic surveys play a central role in
107 constraining V_s structures within shallow marine sediments (e.g., Tsuji et al., 2011).
108 However, in contrast to V_p , investigating V_s via active seismic sources is challenging
109 because of the inefficient excitation of shear waves beneath the seafloor. In recent years,
110 various elements of passive seismic records have been increasingly used to overcome
111 this problem, including ambient surface wave noise (Mosher et al., 2021; Tonegawa et
112 al., 2017; Yamaya et al., 2021; Zhang et al., 2020), teleseismic body waves (Agius et al.,
113 2018; Akuhara et al., 2020), and a combination of them (Doran & Laske, 2019). This
114 study attempts to solve V_s structures through the transdimensional inversion of
115 teleseismic body waves and a surface wave dispersion curve (DC). Based on the results,
116 we discuss the hydrological features in Hyuga-nada, which can be linked to the
117 subducted KPR..

118

119 **2. Passive seismic array**

120 This study uses a passive seismic array of 10 OBSs installed in the Hyuga-nada
121 region. The OBSs continuously recorded seismic waveforms from March 30, 2018, to
122 September 30, 2018 (Figure 1). Five OBSs (HDA01–05) were evenly installed within a
123 radius of 1 km, whereas the other five OBSs (HDA06–10) were placed within 2 km,
124 around the same center. Each OBS contains short-period three-component sensors

125 (LE-3Dlite, Lennartz Electronic GmbH, Germany) and a gimbal to maintain the sensor's
126 horizontality. The seismometer positions were constrained by acoustic positioning from a
127 research vessel. The sensor orientations were determined from the particle motion of
128 teleseismic Rayleigh waves (Sawaki et al., 2022; Stachnik et al., 2012; see text S1, Figure
129 S1, and Table S1 in the supporting information).

130 The array aimed to explore the potential of passive source methods for imaging
131 shallow sediment structures. Another broadband OBS was deployed at the center of the
132 array circle, but we failed to recover it. The array was placed on the refraction seismic
133 survey line such that the tomography model could be used as a reference (Nakanishi et
134 al., 2018; Figure 1). According to this refraction survey, the interface of the Philippine
135 Sea Plate subducts to ~10–11 km depth beneath the array. The seafloor topography is
136 relatively gentle, with a slight slope to the northeast, resulting in a height difference of
137 only ~120 m over the 4 km diameter (**Figure 1b**). Therefore, its effects on surface and
138 body wave propagation are negligible.

139 **3. Method**

140 This section elaborates on procedures we adopted to estimate V_s structures
141 beneath the OBSs. The DC measurements from ambient noise records are described in
142 Section 3.1. In Section 3.2, we describe the procedure we used to retrieve the Green's
143 function (GF) from teleseismic P-waves. Subsequently, the acquired DC and GFs were
144 inverted to one-dimensional (1D) V_s structures using a transdimensional, stochastic
145 inversion scheme, as discussed in Section 3.3.

146

147 **3.1 Rayleigh wave dispersion curve**

148 We retrieved Rayleigh waves propagating across the array from half-year-long
149 records of ambient seismic noise. For this purpose, we employ a series of signal
150 processing steps: cutting records into one-hour-long segments, detrending time series,
151 downsampling data from 200 to 10 samples per second, deconvolution with instrumental
152 responses, spectral whitening, and one-bit normalization in the time domain (Bensen et
153 al., 2007). Cross-correlation functions (CCFs) of vertical components are then calculated
154 between each station pair and stacked over the entire observation period. Figure 2 shows
155 vertical-component CCFs obtained from all station pairs. The fundamental Rayleigh
156 mode dominates CCFs at 0.2–0.4 Hz with an apparent velocity of ~0.5 km/s.

157 Based on the assumption of a laterally homogeneous structure beneath the array,
158 the aggregation of CCFs in Figure 2 can be considered a virtual short gather recorded by
159 a linear array. We estimate an averaged DC across the OBS array by applying the
160 frequency–wavenumber (FK) analysis to this virtual shot gather. This treatment can

161 significantly extend the high-frequency (or short-wavelength) limit of phase velocity
162 measurements without suffering from spatial aliasing effects (Gouédard et al., 2008).
163 This feature benefits this study because acquiring higher-frequency phase velocities is
164 essential to constrain shallow structures of marine sediments.

165 The FK domain spectrum obtained from these virtual records shows the DC of the
166 fundamental Rayleigh wave, which is traceable from 0.15 Hz (near the resolution limit)
167 to 0.5 Hz (**Figure 3**). The DC shows minor deflection at ~ 0.4 Hz, which we consider an
168 artifact from the specific array configuration. In the higher frequency range between
169 0.5–1.0 Hz, the spectrum exhibits a complex pattern, and it is hard to distinguish the
170 actual signal from artificial sidelobes. A relatively continuous feature can be observed at
171 a frequency of >1 Hz, corresponding to the higher-mode Rayleigh wave, but the mode
172 identification is nontrivial because of the ambiguity in the range of 0.5–1.0 Hz.

173

174 **3.2 Teleseismic Green's functions**

175 We extract P waveforms of teleseismic events with $M > 5.5$ and an epicentral
176 distance of $30\text{--}90^\circ$. Each extracted record is decimated to 20 samples per second, and
177 two horizontal components were rotated to radial and transverse directions. We only
178 retain data with a signal-to-noise ratio (SNR) above 3.0 on the vertical component. In
179 this study, the SNR is defined as the root-mean-square amplitude ratio of 30 s time
180 windows before and after P arrival. The GFs of teleseismic P-waves are retrieved from
181 these time windows with the blind deconvolution technique (Akuhara et al., 2019). In
182 contrast to conventional receiver function methods that only solve radial-component
183 GFs, both radial- and vertical-component GFs can be estimated with this method. The
184 retrieval of vertical-component GFs is crucial for ocean-bottom settings because intense
185 water multiples dominate the vertical-component records. We use 60 s time windows for
186 the deconvolution and apply a Gaussian low-pass filter to the results. The Gaussian
187 parameter (i.e., standard deviation) is set to 8, corresponding to a 10% gain at ~ 4 Hz.

188 The radial-component GFs are mostly coherent across the array, especially for the
189 first 4 seconds (Figure 4a; see also Figure S2–S11 for wiggle plots against event back
190 azimuths). A negative peak is predominant at $\sim 2.0\text{--}2.5$ s after the direct P arrival. This
191 coherency quantitatively justifies the 1D structure assumption we made for the FK
192 analysis. At zero lag time, a peak corresponding to the direct P arrival is not evident,
193 indicating the nearly vertical incidence of the P phase due to the low V_p of
194 unconsolidated sediments. The vertical-component GFs show reverberations within the
195 seawater column (Figure 4b). The first reverberation with a positive polarity is evident
196 at 3.1 s, and the second one can be observed at 6.2 s and has a reversed polarity.

197 Although we did not use these vertical-component GFs for the inversion analysis, the
198 good recovery of water reverberations to some degree validates the radial component
199 estimations.

200

201 **3.3 Transdimensional Bayesian inversion**

202 We use a transdimensional Bayesian interface and the reversible-jump Markov
203 chain Monte Carlo (RJMCMC) algorithm (Green, 1995) for the inversion of the
204 dispersion and GF data to an isotropic 1D Vs model beneath each OBS. The RJMCMC
205 performs probabilistic sampling of model parameters, allowing the dimension of the
206 model parameter space to be unknown. In our case, the algorithm automatically selects
207 the number of layers in the 1D subsurface structure model. The transdimensional
208 Bayesian inversion aims to estimate the posterior probability of the model parameter,
209 \mathbf{m}_k , with the given data, \mathbf{d} , that is, $P(k, \mathbf{m}_k | \mathbf{d})$, where k is a parameter determining
210 the model-space dimension. Based on the Bayes' theorem, the posterior probability is
211 proportional to the product of the prior probability, $P(k, \mathbf{m}_k)$, and the likelihood,
212 $P(\mathbf{d} | k, \mathbf{m}_k)$:

$$P(k, \mathbf{m}_k | \mathbf{d}) \propto P(k, \mathbf{m}_k) P(\mathbf{d} | k, \mathbf{m}_k).$$

213

214 *3.3.1 Model parameters*

215 We assume that the subsurface structure consists of k layers. Each layer has
216 constant seismic P- and S-wave velocities and density; the structure's lateral
217 heterogeneity, anisotropy, and dissipation are ignored. We defined a model vector
218 $\mathbf{m}_k = (z_1, \dots, z_{k-1}, \delta\beta_1, \dots, \delta\beta_{k-1}, \sigma_{DC}, \sigma_{GF})^T$, where $\delta\beta_i$ is the S-wave velocity
219 perturbation relative to a reference model and z_i is the bottom depth of the i th layer.
220 The other two parameters, σ_{DC} and σ_{GF} , represent the standard deviations of data
221 noise, which are also solved within the hierarchical Bayesian model (Bodin et al., 2012).
222 Based on a given set of model parameters, first, a Vs value of each layer is extracted
223 from the reference model. The perturbation $\delta\beta_i$ is then added to the extracted value.
224 Similarly, Vp is obtained from the reference model, but without perturbation. The
225 density is calculated from the Vp using an empirical relationship (Brocher, 2005). We
226 fix the properties of the bottom half-space (i.e., k th layer) to stabilize the forward
227 calculation of dispersion curves: Vs is set to 4.0 km/s and Vp and the density are scaled
228 to Vs using the empirical law of Brocher (2005). For the seawater layer, we assume an
229 acoustic velocity of 1.5 km/s and thickness of 2.388 km, which is the average station
230 depth. The reference model was constructed from the two-dimensional (2D) P-wave
231 velocity model of Nakanishi et al. (2008), as shown in Figure 1c, with the empirical

232 scaling law that converts Vp into Vs (Brocher, 2005). Since the lateral velocity variation
 233 is small across the array, we construct a single reference model and apply it to all
 234 stations.

235

236 3.3.2 Likelihood

237 We calculate the likelihood $P(\mathbf{d}|k, \mathbf{m}_k)$ based on the assumption of Gaussian
 238 noise distribution:

$$P(\mathbf{d}|k, \mathbf{m}_k) = P(\mathbf{d}_{DC}|k, \mathbf{m}_k)P(\mathbf{d}_{GF}|k, \mathbf{m}_k),$$

$$P(\mathbf{d}_{DC}|k, \mathbf{m}_k) = \frac{1}{\sqrt{(2\pi)^{N_{DC}}|\mathbf{C}_{DC}|}} \exp\left\{-\frac{1}{2}[\mathbf{g}_{DC}(k, \mathbf{m}_k) - \mathbf{d}_{DC}]^T \mathbf{C}_{DC}^{-1} [\mathbf{g}_{DC}(k, \mathbf{m}_k) - \mathbf{d}_{DC}]\right\}, \#$$

239 and

$$P(\mathbf{d}_{GF}|k, \mathbf{m}_k) = \frac{1}{\sqrt{(2\pi)^{N_{GF}}|\mathbf{C}_{GF}|}} \exp\left\{-\frac{1}{2}[\mathbf{g}_{GF}(k, \mathbf{m}_k) - \mathbf{d}_{GF}]^T \mathbf{C}_{GF}^{-1} [\mathbf{g}_{GF}(k, \mathbf{m}_k) - \mathbf{d}_{GF}]\right\}, \#$$

240 where \mathbf{C}_{DC} and \mathbf{C}_{GF} are the covariance matrices of the DC and GF data noise,
 241 respectively, and \mathbf{g}_{DC} and \mathbf{g}_{GF} are the synthetic DC and GF, respectively. The data
 242 vector, \mathbf{d} , consists of DC and GF data vectors, denoted as \mathbf{d}_{DC} and \mathbf{d}_{GF} , respectively,
 243 with a length of N_{DC} and N_{GF} , respectively. We assume the temporal correlation of
 244 noise for GFs, which originates from the Gaussian low-pass filter, and a constant noise
 245 level across the entire time series. The corresponding covariance matrix can be
 246 expressed by $C_{GFij} = \sigma_{GF}^2 r^{(j-i)^2}$, where r is pre-determined from the Gaussian filter
 247 width (Bodin et al., 2012) and σ_{GF} is a standard deviation of the data noise. We ignore
 248 off-diagonal components of the DC covariance matrix and assumed
 249 frequency-independent measurement error, which results in $C_{DCij} = \sigma_{DC}^2 \delta_{ij}$, where σ_{DC}
 250 is a standard deviation of DC data noise and δ_{ij} is the Kronecker delta. The standard
 251 deviations (i.e., σ_{DC} and σ_{GF}) are treated as hyper parameters and solved together with
 252 the model parameters (Bodin et al., 2012).

253

254 3.3.3. Prior probabilities

255 We assume truncated uniform distributions for the prior probability of k , σ_{DC} ,
 256 and σ_{GF} . We also assume the following limits: $[k_{min}, k_{max}] = [1, 51]$ for k ,
 257 $[\sigma_{DCmin}, \sigma_{DCmax}] = [0.005, 0.090]$ for σ_{DC} (unit in km/s), and $[\sigma_{GFmin}, \sigma_{GFmax}] =$
 258 $[0.02, 0.07]$ for σ_{GF} . We tested several choices for these parameters to find that the
 259 resulting velocity structures did not change significantly. We set the minimum limit of
 260 the layer depths to $z_{min} = 2.388$ (water depth) and the maximum to $z_{max} = 15$ km and

261 use the Dirichlet partition prior with unit concentration parameters (Dosso et al., 2014).
 262 This setting corresponds to a non-informative prior: the prior probability remains
 263 constant no matter where the layer boundary is between z_{min} and z_{max} . We use the
 264 Gaussian distribution with a zero mean for the Vs anomalies. The Gaussian width (i.e.,
 265 standard deviation $\sigma_{\delta\beta}$) must reflect how reliable the reference model is. We set this
 266 parameter to 0.2 km/s. In summary, the joint prior can be expressed as follows:

$$P(k, \mathbf{m}_k) = \frac{1}{k_{max} - k_{min}} \cdot \frac{1}{\sigma_{DCmax} - \sigma_{DCmin}} \cdot \frac{1}{\sigma_{GFmax} - \sigma_{GFmin}} \cdot \frac{k!}{(z_{max} - z_{min})^k} \cdot \prod_{i=1}^{k-1} \frac{1}{\sigma_{\delta\beta} \sqrt{2\pi}} \exp\left(-\frac{\delta\beta_i^2}{2\sigma_{\delta\beta}^2}\right).$$

267 We confirmed that our inversion code implements the prior probability as intended by
 268 performing MCMC, forcing the likelihood to be zero (Figure S12).

269

270 3.3.4. Probabilistic sampling with parallel tempering

271 The RJMCMC algorithm aims to sample the posterior probability $P(k, \mathbf{m}_k | \mathbf{d})$
 272 through iteration. At each iteration, a new model $(k', \mathbf{m}'_{k'})$ is proposed by either (1)
 273 adding a layer, (2) removing a layer, (3) moving a layer interface, (4) perturbing the
 274 S-wave velocity of a layer, or (5) perturbing the standard deviation of the data noise.
 275 One of the above-mentioned five procedures is randomly selected at each iteration to
 276 generate a new model. The proposed model is accepted at a probability α_{MHG} , which is
 277 defined as the tempered Metropolis–Hastings–Green criterion (Green, 1995):

$$\alpha_{MHG} = \min \left\{ 1, \frac{P(k', \mathbf{m}'_{k'}) \left[\frac{P(\mathbf{d} | k', \mathbf{m}'_{k'})}{P(\mathbf{d} | k, \mathbf{m}_k)} \right]^{\frac{1}{T}} \frac{Q(k, \mathbf{m}_k | k', \mathbf{m}'_{k'})}{Q(k', \mathbf{m}'_{k'} | k, \mathbf{m}_k)} |\mathbf{J}| \right\}, \#$$

278 where $P(k, \mathbf{m}_k)$ is the prior probability; $Q(k', \mathbf{m}'_{k'} | k, \mathbf{m}_k)$ is the probability that a
 279 transition from (k, \mathbf{m}_k) to $(k', \mathbf{m}'_{k'})$ is proposed, and $|\mathbf{J}|$ is the Jacobian
 280 compensating for a unit volume change in the model space. The exponent $T (> 1)$,
 281 which represents a temperature that loses the acceptance criterion, is a modification of
 282 the original Metropolis–Hastings–Green criterion. In the parallel tempering method
 283 (Geyer & Thompson, 1995; Sambridge, 2014), differently tempered Markov chains are
 284 run in parallel. At the end of each iteration, 10 pairs of chains are probabilistically
 285 allowed to swap the temperatures. Based on this swap, the random walk can undergo a
 286 long jump in the model space and efficiently converge to the global maximum.

287 The inversion involves 1,000,000 iterations, including the first 800,000 iterations
 288 of the burn-in period. In total, 100 Markov chains are run in parallel, 20 of which have a

289 unit temperature and are used to evaluate posterior probabilities. We only save the
290 models every 2,000 iterations to avoid artificial correlation between samples.

291

292 4. Results

293 The ensemble of model parameters sampled by the transdimensional inversion
294 provides insights into the probable range of a 1D V_s structure beneath each station.
295 Figure 5 shows the inversion results obtained at HDA06. The posterior marginal
296 probability of V_s as a function of depth indicates a well-converged solution with a
297 clearly defined peak at each depth. Other diagnostic information, such as the evolution
298 of log-likelihood and acceptance ratio of proposals, is shown in Figure S13 and Table
299 S2, respectively. According to the mode value at each 0.3 km depth (green line, Figure
300 5), the velocity increases up to a depth of 4.8 km, with sharp, positive velocity contrasts
301 at depths of 2.7 and 3.9 km. Although less clear, these discontinuities can be seen in the
302 maximum a posteriori (MAP) estimate (purple line, Figure 5). We conclude that these
303 contrasts reflect different lithologies of sediments and refer to the layers as sedimentary
304 units 1–3 (U1–3), from top to bottom.

305 Beneath this unit sequence, V_s abruptly drops to form a LVZ. The top of the LVZ
306 is 0.1 km deeper than the depth at which the referenced V_p tomography model exhibits
307 velocity inversion. Note that our prior V_s information already incorporates the velocity
308 inversion that can be observed in the V_p model (black curve, Figure 5f). The inversion
309 analysis requires the further reduction of V_s , suggesting a high V_p/V_s ratio in the LVZ:
310 based on the assumption of a V_p of 3.4 km/s from the V_p tomography model, the V_p/V_s
311 ratio corresponds to 2.8. However, this estimation likely overestimates V_p/V_s ratio. This
312 is because the reference V_p tomography model has a coarser vertical resolution than V_s
313 profiles obtained in this study, subject to smoothing constraints. Thus, we smoothed the
314 V_s profile using a running window of 1.5 km depth to mimic the vertical resolution of
315 seismic tomography (Figure S14). The window length of 1.5 km was chosen by trial and
316 error so that V_s profile exhibits a similar degree of smoothness to the reference V_p
317 model. Even after this smoothing, the V_p/V_s profile culminates at the LVZ with a
318 maximum value of 2.5.

319 Inversion results from other stations show similar first-order features. Three
320 layers (i.e., U1–3) are discernible immediately beneath the seafloor, and a LVZ can be
321 detected beneath them, especially evident with mode estimations (Figure 6). An
322 exception is HDA01 without a LVZ. This absence of LVZ beneath HAD01 could be
323 artificial, considering that V_s profiles from the other stations consistently exhibit a LVZ.
324 Since the LVZ is the center of interest, we exclude HDA01 results from the discussion

325 for simplicity. Following the last paragraph, we calculate smoothed V_p/V_s profiles of
326 each station. The resulting V_p/V_s profile shows a peak at the LVZ depth for most
327 stations (Figure 7). The peak values from mode estimations are consistent among
328 HDA02, 03, 04, 05, 06, 08, and 09, ranging from 2.5–2.7. Stations HDA07 and HDA10
329 show relatively lower V_p/V_s , 2.2 and 2.0, respectively, but the probability distribution
330 of those stations has an elongated tail toward higher V_p/V_s . Thus, the V_p/V_s ratio of
331 2.5–2.7 may also be applicable to these two stations.

332 To quantify the depth of each lithological boundary, we searched for the depth of
333 maximum velocity contrast within a given depth range. This search was performed for
334 all 1D S-wave velocity structures sampled in the inversion. The aggregation of all
335 results provides statistics for the lithological boundary depths. We set depth ranges for
336 this search to 2.3–3.1 km for the boundary U1–U2, 3.1–5.5 km for U2–U3, 4.0–7.0 km
337 for U3–LVZ, and 5.5–9.5 km for the bottom of the LVZ. The resulting median estimates
338 are shown as background colors in Figures 6 and 7. In addition, 68% confidence
339 intervals are shown in Figure 8b. Note that this error estimation tends to be biased
340 toward magnifying uncertainties because the transdimensional inversion can produce
341 ineffective (i.e., too thin) layers at random depths with a considerable velocity contrast.
342 Hence, we chose to display the 68% confidence intervals in Figure 8b rather than the
343 commonly used 95% intervals.

344 The above qualitative estimates of uncertainties confirmed the lateral variation in
345 the depth of the top of the LVZ: the lithological boundary deepens on the southwestern
346 side, whereas it becomes shallower on the northeastern side (Figure 8a). The depth
347 offset is sharp: ~ 1 km vertical offset within a distance of 0.5 km. The green vertical bars
348 in Figure 8c show a 68% range of theoretical arrivals of the Ps converted phase from the
349 top of the LVZ, which is drawn from MCMC samples. For all stations except HDA03,
350 these timings predict a negative phase arrival well. The negative phase arrives at the
351 northeastern stations (HDA06, 02, 08, and 07) ~ 0.5 s earlier than at the southwestern
352 stations (HDA10, 09, 04, and 05). This offset in the time domain must be responsible
353 for the offset in the depth domain. For HDA03, the theoretical arrival does not match
354 negative phase arrivals. Multiple reflections from the shallower layers may overprint a
355 Ps phase from the top of the LVZ.

356 The present study fixes a P-wave velocity structure at a single reference model
357 and applies it to all stations, ignoring the presence of lateral heterogeneities and
358 uncertainties in the reference model. However, such a fixed V_p could minorly bias V_s
359 estimation because P-wave GFs (or receiver functions) have secondary sensitivity to
360 V_p/V_s ratios (e.g., Zhu, L., Kanamori, 2000). To quantify this effect, we solved V_p

361 anomalies as well as Vs, where a Gaussian distribution with a standard deviation of 0.15
362 km/s is used as the prior probability for Vp anomaly. The results show that the main
363 feature (i.e., the LVZ) does not change, irrespective of whether Vp is solved (Figure
364 S15). The posterior probability of Vp remains nearly identical to the prior probability
365 below a depth of 4 km, suggesting that the dataset is only sensitive to the shallow part
366 of the Vp structure. The longer time window of GFs could constrain Vp/Vs ratios of the
367 LVZ, but unfortunately, GFs do not show good consistency for phases arriving later than
368 4 s (see Figure 4a).

369 Another concern is overfitting. The transdimensional inversion could
370 unnecessarily add many thin layers to cause overinterpretation of input data. In theory,
371 this issue can be avoided by the adopted transdimensional inversion scheme but could
372 occur with an inappropriate parameterization made for the likelihood, for example. To
373 see whether the obtained LVZ is robust, we enforced a smaller number of layers by
374 setting k_{max} to 21. Still, we observe an evident LVZ (Figure S16). As another test case,
375 we conducted a fixed-dimensional inversion by fixing k at 20. The other parameters,
376 including layer depths, are allowed to vary freely. We found that this fixed-dimensional
377 setting fails to reach a well-converged solution, highlighting the efficient model search
378 by the transdimensional algorithm (Figure S17). This kind of advantage in the
379 transdimensional scheme has not been discussed elsewhere, to the best knowledge, but
380 should be investigated more in the future.

381

382 **5. Geological interpretation**

383 The inversion results present a remarkable low-velocity, high Vp/Vs feature with
384 a velocity inversion. Typically, marine sediments undergo a monotonic increase in Vs
385 with increasing depth because of compaction (Hamilton, 1979). The velocity inversion
386 observed in this study is unexpected. A plausible cause for the observed velocity
387 inversion is high pore fluid pressure. Based on theory and experiments, it is known that
388 high pore fluid pressure increases the Vp/Vs ratio of marine sediments (Dvorkin et al.,
389 1999; Prasad, 2002), which agrees with our results. Therefore, we interpret that the LVZ
390 represents a fluid reservoir. Aligned cracks could also explain the high Vp/Vs ratio even
391 in the absence of fluid through anisotropic effects (X. Q. Wang et al., 2012). However,
392 we find that numerical modeling based on a scattering theory with penny-shaped
393 parallel cracks (Hudson, 1981) fails to explain such high Vp/Vs ratios (2.5–2.6), at least
394 within the reasonable range of crack density (<0.1 ; Crampin & Leary, 1993). For this
395 modeling, we assume an isotropic host rock with a Vp of 3.6 km/s, Vs of 2.0 km/s, and
396 density of 2.3 g/cm³. Those values are extracted from Unit 3.

397 Sustaining the overpressure condition within the fluid reservoir will require a
398 relatively impermeable structure above. Laboratory measurements on terrigenous
399 sediments from deep-sea drilling have shown that the porosities gradually decrease with
400 depth, from ~70% at the sea bottom to ~20% at a burial depth of 1.5 km (Kominz et al.,
401 2011). It has also been reported that porosity changes from 70% to 20% for mudrocks
402 correspond to a 3–4 orders of magnitude decrease in permeability (Neuzil, 1994) . Thus,
403 we speculate that the bottom of Unit 3, with a burial depth of ~2.6–3.9 km, undergoes
404 more severe porosity loss and can impede fluid to permeate shallower layers. This
405 permeability barrier could trap abundant fluid below, leading to the formation of the
406 fluid reservoir.

407 Considering the shallow subduction depth (~ 10 km), subducted sediment along
408 with the Phillippine Sea plate is likely a fluid source, which can release fluid via
409 mechanical compaction or dehydration (Saffer & Tobin, 2011). The occurrence of slow
410 earthquakes may reflect fluid-rich conditions near the subducting plate interface: lines
411 of evidence require high pore fluid pressure for the genesis of slow earthquakes (Behr &
412 Bürgmann, 2021 and references therein). Since this possible fluid source is spatially
413 separated from the LVZ, permeable structures such as faults or fractures will be required
414 to effectively convey fluids from the subducted sediments to the LVZ, as discussed in
415 the next paragraph. Such permeable structures may not penetrate Unit 3. After reaching
416 the bottom of Unit 3, fluids might diffuse laterally in accordance with permeability
417 anisotropy due to sediment stratification.

418 The presence of faults in the overriding prism seems natural for this region with
419 the subducted KPR. Analog and numerical experiments have demonstrated that many
420 back-thrusts occur on the leading flank of the seamount (Dominguez et al., 1998; Sun et
421 al., 2020). A recent compilation of seismic reflection surveys in the Hyuga-nada has
422 identified several NNW–SSE trending thrust faults northeast to the array (Figure 9;
423 Headquarters for Earthquake Research Promotion, 2020). At ~2 Ma, before the last
424 change in the convergence direction, the KPR was located east of the present position
425 (Mahony et al., 2011). The subsequent oblique subduction involves right-lateral motion
426 along the trench, potentially inducing the northeast-dipping back-thrust near the array
427 (Figure 10a). Notably, this fault trend is roughly parallel to the sharp offset in the LVZ
428 depth we observed. The sharp offset could imply the presence of a blind back-thrust
429 fault beneath it. Cumulative deformation along the fault might be responsible for the
430 sharp offset. If existing, such a fault will act as a fluid conduit (Figure 10a).

431 We acknowledge that our dataset poses only weak constraints on the geological
432 process behind the LVZ and thus does not exclude other possibilities. For another

433 hypothesis, the LVZ could represent ascending, overpressured material, such as a mud
434 diapir (e.g., Brown, 1990), about to pierce into Unit 3 (Figure 10b). The head of
435 ascending body would selectively intrude into Unit 3 along a mechanically weakened
436 fabric parallel to the KPR, which leads to the NNW-SSE trending depth offset.
437 Similarly oriented faults nearby the array (Figure 9) support the presence of such a weak
438 fabric. Further investigation in combination with active-source seismic surveys can
439 illuminate the cause of this LVZ but is left for our future work.

440 This study has identified that the LVZ extends laterally, at least to the array size
441 (~4 km). The V_p gradient profile shown in Figure 1d suggests that the LVZ extends ~60
442 km laterally beyond the aperture of the OBS array. Moreover, an independent seismic
443 refraction profile in Hyuga-nada has obtained a comparable low-velocity feature within
444 the accretionary prism, ~50–100 km south of the array (Nishizawa et al., 2009),
445 possibly suggesting that similar fluid reservoirs are widely distributed in this region.
446 Pursuing its spatial extent will be important for better understanding the cause of the
447 LVZ and hydrological processes of Hyuga-nada in association with the KPR.

448

449 **6. Conclusions**

450 In this study, the V_s structure in the Hyuga-nada accretionary prism was
451 constrained using a passive seismic array. The V_s structure exhibits a LVZ beneath
452 stratified sedimentary units (U1–3). Based on the reduced V_s and high V_p/V_s ratio, we
453 conclude that the LVZ reflects a fluid reservoir with high pore fluid pressure sustained
454 by the impermeable layering above. The significant depth offset of the top of the LVZ,
455 extending over ~4 km of the array aperture, possibly suggests the presence of a blind
456 thrust fault or fractures. Such faults generated by the subduction of the KPR may act as
457 fluid pathways and contribute to the reservoir. However, we do not exclude other
458 possibilities: the LVZ may reflect a mud diapir, for example.

459 The results of this study demonstrate the potential of passive seismic source
460 analyses to acquire a high-resolution structure of V_s , leading to gaining new constraints
461 on fluid processes in the accretionary system. A limitation is its narrow resolvable range
462 laterally, which may hamper interpreting resultant V_s structures conclusively. Joint
463 interpretation with active seismic source surveys will remedy this drawback. Nowadays,
464 a number of seismic survey data have been obtained in subduction zones worldwide.
465 Additional passive seismic experiments like this study will help understand physical
466 properties and hydrological features in the accretionary prism.

467

468 **Acknowledgments**

469 We thank three anonymous reviewers for their constructive comments. We also
470 thank Ryuta Arai for his valuable discussion, which helped conceptualize this study.
471 This study was supported by JSPS KAKENHI Grant Number 19K14811 and by the
472 Ministry of Education, Culture, Sports, Science and Technology (MEXT) of Japan,
473 under its Earthquake and Volcano Hazards Observation and Research Program.

474

475 **Data availability**

476 The teleseismic P-waves and ambient noise cross-correlation functions used in
477 this study is available at Zenodo repository (<https://doi.org/10.5281/zenodo.7344432>). A
478 computer program for the deconvolution of teleseismic waveforms is available at
479 GitHub repository (<https://github.com/akuhara/MC3deconv>) or Zenodo repository
480 (<https://doi.org/10.5281/zenodo.2548974>). A computer program for transdimensional
481 inversion is available at GitHub repository (https://github.com/akuhara/SEIS_FILO) or
482 Zenodo repository (<https://doi.org/10.5281/zenodo.6330840>). The Vp models of
483 Nakanishi et al. (2018) are available upon request through the JAMSTEC Seismic
484 Survey Database (JAMSTEC, 2004).

485

486 **References**

- 487 Agius, M. R., Harmon, N., Rychert, C. A., Tharimena, S., & Kendall, J. M. (2018).
488 Sediment Characterization at the Equatorial Mid-Atlantic Ridge From P-to-S
489 Teleseismic Phase Conversions Recorded on the PI-LAB Experiment. *Geophysical*
490 *Research Letters*, *45*(22), 12,244-12,252. <https://doi.org/10.1029/2018GL080565>
- 491 Akuhara, T., Bostock, M. G., Plourde, A. P., & Shinohara, M. (2019). Beyond Receiver
492 Functions: Green's Function Estimation by Transdimensional Inversion and Its
493 Application to OBS Data. *Journal of Geophysical Research: Solid Earth*, *124*(2),
494 1944–1961. <https://doi.org/10.1029/2018JB016499>
- 495 Akuhara, T., Tsuji, T., & Tonegawa, T. (2020). Overpressured Underthrust Sediment in
496 the Nankai Trough Forearc Inferred From Transdimensional Inversion of High-
497 Frequency Teleseismic Waveforms. *Geophysical Research Letters*, *47*(15).
498 <https://doi.org/10.1029/2020GL088280>
- 499 Arnulf, A. F., Biemiller, J., Lavier, L., Wallace, L. M., Bassett, D., Henrys, S., et al.
500 (2021). Physical conditions and frictional properties in the source region of a
501 slow-slip event. *Nature Geoscience*, *14*(5), 334–340.
502 <https://doi.org/10.1038/s41561-021-00741-0>
- 503 Baba, S., Takemura, S., Obara, K., & Noda, A. (2020). Slow Earthquakes Illuminating
504 Interplate Coupling Heterogeneities in Subduction Zones. *Geophysical Research*

505 *Letters*, 47(14), 4–5. <https://doi.org/10.1029/2020GL088089>

506 Behr, W. M., & Bürgmann, R. (2021). *What's down there? The structures, materials and*
507 *environment of deep-seated slow slip and tremor. Philosophical Transactions of*
508 *the Royal Society A: Mathematical, Physical and Engineering Sciences* (Vol. 379).
509 <https://doi.org/10.1098/rsta.2020.0218>

510 Bensen, G. D., Ritzwoller, M. H., Barmin, M. P., Levshin, A. L., Lin, F., Moschetti, M. P.,
511 et al. (2007). Processing seismic ambient noise data to obtain reliable broad-band
512 surface wave dispersion measurements. *Geophysical Journal International*, 169(3),
513 1239–1260. <https://doi.org/10.1111/j.1365-246X.2007.03374.x>

514 Bodin, T., Sambridge, M., Tkalčić, H., Arroucau, P., Gallagher, K., & Rawlinson, N.
515 (2012). Transdimensional inversion of receiver functions and surface wave
516 dispersion. *Journal of Geophysical Research: Solid Earth*, 117(2), 1–24.
517 <https://doi.org/10.1029/2011JB008560>

518 Brocher, T. M. (2005). Empirical relations between elastic wavespeeds and density in the
519 Earth's crust. *Bulletin of the Seismological Society of America*, 95(6), 2081–2092.
520 <https://doi.org/10.1785/0120050077>

521 Brown, K. M. (1990). The nature and hydrogeologic significance of mud diapirs and
522 diatremes for accretionary systems. *Journal of Geophysical Research*, 95(B6),
523 8969. <https://doi.org/10.1029/JB095iB06p08969>

524 Chesley, C., Naif, S., Key, K., & Bassett, D. (2021). Fluid-rich subducting topography
525 generates anomalous forearc porosity. *Nature*, 595(7866), 255–260.
526 <https://doi.org/10.1038/s41586-021-03619-8>

527 Crampin, S., & Leary, P. C. (1993). Limits to crack density: The state of fractures in
528 crustal rocks. In *SEG Technical Program Expanded Abstracts 1993* (pp. 758–761).
529 Society of Exploration Geophysicists. <https://doi.org/10.1190/1.1822609>

530 Van Dinther, Y., Gerya, T. V., Dalguer, L. A., Mai, P. M., Morra, G., & Giardini, D.
531 (2013). The seismic cycle at subduction thrusts: Insights from seismo-thermo-
532 mechanical models. *Journal of Geophysical Research: Solid Earth*, 118(12),
533 6183–6202. <https://doi.org/10.1002/2013JB010380>

534 Dominguez, S., Lallemand, S., Malavieille, J., & von Huene, R. (1998). Upper plate
535 deformation associated with seamount subduction. *Tectonophysics*, 293(3–4),
536 207–224. [https://doi.org/10.1016/S0040-1951\(98\)00086-9](https://doi.org/10.1016/S0040-1951(98)00086-9)

537 Doran, A. K., & Laske, G. (2019). Seismic Structure of Marine Sediments and Upper
538 Oceanic Crust Surrounding Hawaii. *Journal of Geophysical Research: Solid Earth*,
539 124(2), 2038–2056. <https://doi.org/10.1029/2018JB016548>

540 Dosso, S. E., Dettmer, J., Steininger, G., & Holland, C. W. (2014). Efficient

541 trans-dimensional Bayesian inversion for geoacoustic profile estimation. *Inverse*
542 *Problems*, 30(11), 114018. <https://doi.org/10.1088/0266-5611/30/11/114018>

543 Dvorkin, J., Mavko, G., & Nur, A. (1999). Overpressure detection from compressional-
544 and shear-wave data. *Geophysical Research Letters*.
545 <https://doi.org/10.1029/1999GL008382>

546 Geyer, C. J., & Thompson, E. A. (1995). Annealing Markov Chain Monte Carlo with
547 Applications to Ancestral Inference. *J. Am. Stat. Assoc.*, 90(431), 909–920.
548 <https://doi.org/10.1080/01621459.1995.10476590>

549 Gouédard, P., Cornou, C., & Roux, P. (2008). Phase-velocity dispersion curves and
550 small-scale geophysics using noise correlation slantstack technique. *Geophysical*
551 *Journal International*, 172(3), 971–981.
552 <https://doi.org/10.1111/j.1365-246X.2007.03654.x>

553 Green, P. J. (1995). Reversible jump Markov chain monte carlo computation and
554 Bayesian model determination. *Biometrika*, 82(4), 711–732.
555 <https://doi.org/10.1093/biomet/82.4.711>

556 Hamilton, E. L. (1979). V_p / V_s and Poisson's ratios in marine sediments and rocks.
557 *The Journal of the Acoustical Society of America*, 66(4), 1093–1101.
558 <https://doi.org/10.1121/1.383344>

559 Headquarters for Earthquake Research Promotion (2020). Comprehensive assessment of
560 fault information in marine areas (in Japanese). Retrieved from
561 https://www.jishin.go.jp/main/chousakenkyuu/kaiiki/r01/R01kaiiki_3_2.pdf

562 Hudson, J. A. (1981). Wave speeds and attenuation of elastic waves in material
563 containing cracks. *Geophysical Journal of the Royal Astronomical Society*, 64(1),
564 133–150. <https://doi.org/10.1111/j.1365-246X.1981.tb02662.x>

565 Itoh, Y., Takemura, K., & Kamata, H. (1998). History of basin formation and tectonic
566 evolution at the termination of a large transcurrent fault system: deformation mode
567 of central Kyushu, Japan. *Tectonophysics*, 284(1–2), 135–150.
568 [https://doi.org/10.1016/S0040-1951\(97\)00167-4](https://doi.org/10.1016/S0040-1951(97)00167-4)

569 JAMSTEC. (2004). JAMSTEC Seismic Survey Database.
570 <https://doi.org/10.17596/0002069>

571 Kominz, M. A., Patterson, K., & Odette, D. (2011). Lithology dependence of porosity in
572 slope and deep marine sediments. *Journal of Sedimentary Research*, 81(10), 730–
573 742. <https://doi.org/10.2110/jsr.2011.60>

574 Mahony, S. H., Wallace, L. M., Miyoshi, M., Villamor, P., Sparks, R. J., & Hasenaka, T.
575 (2011). Volcano-tectonic interactions during rapid plate-boundary evolution in the
576 Kyushu region, SW Japan. *Bulletin of the Geological Society of America*, 123(11–

577 12), 2201–2223. <https://doi.org/10.1130/B30408.1>

578 Mosher, S. G., Eilon, Z., Janiszewski, H., & Audet, P. (2021). Probabilistic inversion of
579 seafloor compliance for oceanic crustal shear velocity structure using mixture
580 density neural networks. *Geophysical Journal International*, 227(3), 1879–1892.
581 <https://doi.org/10.1093/gji/ggab315>

582 Nakanishi, A., Takahashi, N., Yamamoto, Y., Takahashi, T., Ozgur Citak, S., Nakamura,
583 T., et al. (2018). Three-dimensional plate geometry and P-wave velocity models of
584 the subduction zone in SW Japan: Implications for seismogenesis. In T. Byrne, I.
585 Underwood, Michael B., D. Fisher, L. McNeill, D. Saffer, K. Ujiie, & A.
586 Yamaguchi (Eds.), *Geology and Tectonics of Subduction Zones: A Tribute to Gaku*
587 *Kimura*. Geological Society of America. [https://doi.org/10.1130/2018.2534\(04\)](https://doi.org/10.1130/2018.2534(04))

588 Neuzil, C. E. (1994). How permeable are clays and shales? *Water Resources Research*,
589 30(2), 145–150. <https://doi.org/10.1029/93WR02930>

590 Nishizawa, A., Kaneda, K., & Oikawa, M. (2009). Seismic structure of the northern end
591 of the Ryukyu Trench subduction zone, southeast of Kyushu, Japan. *Earth, Planets*
592 *and Space*, 61(8), e37–e40. <https://doi.org/10.1186/bf03352942>

593 Park, J. O., Hori, T., & Kaneda, Y. (2009). Seismotectonic implications of the
594 Kyushu-Palau ridge subducting beneath the westernmost Nankai forearc. *Earth,*
595 *Planets and Space*, 61(8), 1013–1018. <https://doi.org/10.1186/BF03352951>

596 Prasad, M. (2002). Acoustic measurements in unconsolidated sands at low effective
597 pressure and overpressure detection. *Geophysics*, 67(2), 405–412.
598 <https://doi.org/10.1190/1.1468600>

599 Saffer, D. M., & Tobin, H. J. (2011). Hydrogeology and Mechanics of Subduction Zone
600 Forearcs: Fluid Flow and Pore Pressure. *Annual Review of Earth and Planetary*
601 *Sciences*, 39(1), 157–186. <https://doi.org/10.1146/annurev-earth-040610-133408>

602 Saffer, D. M., & Wallace, L. M. (2015). The frictional, hydrologic, metamorphic and
603 thermal habitat of shallow slow earthquakes. *Nature Geoscience*, 8(8), 594–600.
604 <https://doi.org/10.1038/ngeo2490>

605 Sahling, H., Masson, D. G., Ranero, C. R., Hühnerbach, V., Weinrebe, W., Klauke, I., et
606 al. (2008). Fluid seepage at the continental margin offshore Costa Rica and
607 southern Nicaragua. *Geochemistry, Geophysics, Geosystems*, 9(5).
608 <https://doi.org/10.1029/2008GC001978>

609 Sambridge, M. (2014). A Parallel Tempering algorithm for probabilistic sampling and
610 multimodal optimization. *Geophysical Journal International*, 196(1), 357–374.
611 <https://doi.org/10.1093/gji/ggt342>

612 Sawaki, Y., Yamashita, Y., Ohyanagi, S., Garcia, E. S. M., Ito, A., Sugioka, H., et al.

613 (2022). Seafloor depth controls seismograph orientation uncertainty. *Geophysical*
614 *Journal International*. <https://doi.org/10.1093/gji/ggac397>

615 Stachnik, J. C., Sheehan, A. F., Zietlow, D. W., Yang, Z., Collins, J., & Ferris, A. (2012).
616 Determination of New Zealand Ocean Bottom Seismometer Orientation via
617 Rayleigh-Wave Polarization. *Seismological Research Letters*, 83(4), 704–713.
618 <https://doi.org/10.1785/0220110128>

619 Sun, T., Saffer, D., & Ellis, S. (2020). Mechanical and hydrological effects of seamount
620 subduction on megathrust stress and slip. *Nature Geoscience*, 13(3), 249–255.
621 <https://doi.org/10.1038/s41561-020-0542-0>

622 Tonegawa, T., Araki, E., Kimura, T., Nakamura, T., Nakano, M., & Suzuki, K. (2017).
623 Sporadic low-velocity volumes spatially correlate with shallow very low frequency
624 earthquake clusters. *Nature Communications*, 8(1), 2048.
625 <https://doi.org/10.1038/s41467-017-02276-8>

626 Tonegawa, T., Yamashita, Y., Takahashi, T., Shinohara, M., Ishihara, Y., Kodaira, S., &
627 Kaneda, Y. (2020). Spatial relationship between shallow very low frequency
628 earthquakes and the subducted Kyushu-Palau Ridge in the Hyuga-nada region of
629 the Nankai subduction zone. *Geophysical Journal International*, 222(3), 1542–
630 1554. <https://doi.org/10.1093/gji/ggaa264>

631 Tsuji, T., Dvorkin, J., Mavko, G., Nakata, N., Matsuoka, T., Nakanishi, A., et al. (2011).
632 V P / V S ratio and shear-wave splitting in the Nankai Trough seismogenic zone:
633 Insights into effective stress, pore pressure, and sediment consolidation.
634 *Geophysics*, 76(3), WA71–WA82. <https://doi.org/10.1190/1.3560018>

635 Wang, K., & Hu, Y. (2006). Accretionary prisms in subduction earthquake cycles : The
636 theory of dynamic Coulomb wedge, *III*(March), 1–16.
637 <https://doi.org/10.1029/2005JB004094>

638 Yamagishi, Y., Nakanishi, A., Miura, S., Kodaira, S., & Sakaguchi, H. (2018).
639 Development of a database and visualization system integrating various models of
640 seismic velocity structure and subducting plate geometry around Japan. *Progress*
641 *in Earth and Planetary Science*, 5(1). <https://doi.org/10.1186/s40645-018-0207-4>

642 Yamamoto, Y., Obana, K., Takahashi, T., Nakanishi, A., Kodaira, S., & Kaneda, Y.
643 (2013). Imaging of the subducted kyushu-palau ridge in the hyuga-nada region,
644 western nankai trough subduction zone. *Tectonophysics*, 589, 90–102.
645 <https://doi.org/10.1016/j.tecto.2012.12.028>

646 Yamashita, Y., Yakiwara, H., Asano, Y., Shimizu, H., Uchida, K., Hirano, S., et al.
647 (2015). Migrating tremor off southern Kyushu as evidence for slow slip of a
648 shallow subduction interface. *Science*, 348(6235), 676–679.

649 <https://doi.org/10.1126/science.aaa4242>
650 Yamashita, Y., Shinohara, M., & Yamada, T. (2021). Shallow tectonic tremor activities
651 in Hyuga-nada, Nankai subduction zone, based on long-term broadband ocean
652 bottom seismic observations. *Earth, Planets and Space*, 73(1).
653 <https://doi.org/10.1186/s40623-021-01533-x>
654 Yamaya, L., Mochizuki, K., Akuhara, T., & Nishida, K. (2021). Sedimentary Structure
655 Derived From Multi-Mode Ambient Noise Tomography With Dense OBS
656 Network at the Japan Trench. *Journal of Geophysical Research: Solid Earth*,
657 126(6), 1–20. <https://doi.org/10.1029/2021JB021789>
658 Yamazaki, T., & Okamura, Y. (1989). Subducting seamounts and deformation of
659 overriding forearc wedges around Japan. *Tectonophysics*, 160(1–4), 207–229.
660 [https://doi.org/10.1016/0040-1951\(89\)90392-2](https://doi.org/10.1016/0040-1951(89)90392-2)
661 Zhang, X., Hansteen, F., Curtis, A., & de Ridder, S. (2020). 1-D, 2-D, and 3-D Monte
662 Carlo Ambient Noise Tomography Using a Dense Passive Seismic Array Installed
663 on the North Sea Seabed. *Journal of Geophysical Research: Solid Earth*, 125(2),
664 1–32. <https://doi.org/10.1029/2019JB018552>
665 Zhu, L., Kanamori, H. (2000). Moho depth variation in southern California. *Journal of*
666 *Geophysical Research*, 105, 2969–2980. <https://doi.org/10.1029/1999JB900322>
667
668

669 **Figure legends**

670

671 **Figure 1.** Tectonic setting of the study area and array configuration. (a) The orange star
672 denotes the location of an array of ocean-bottom seismometers. The red line represents
673 the cross-section shown in (c) and (d). Yellow dots represent the epicenters of the
674 tectonic tremors (Yamashita et al., 2015, 2021). The pink line denotes the subducted
675 Kyushu-Palau Ridge (Yamamoto et al., 2013). (b) Array configuration. The gray
676 contour indicates the water depth, with an interval of 10 m. (c) P-wave velocity model
677 obtained from a refraction survey (Nakanishi et al., 2018). The yellow inverse triangles
678 represent the locations of ocean-bottom seismometers. The subducting plate interface is
679 denoted by the black line, which is defined by the velocity gradient profile of (d). (d)
680 The same as (c), but vertical velocity gradients are shown. PHP: Philippine Sea Plate.

681

682 **Figure 2.** Ambient noise cross-correlation functions filtered from 0.2 to 0.4 Hz.
683 Cross-correlation functions from all pairs of stations are displayed against their
684 inter-station distances. The green line corresponds to a propagation speed of 0.5 km/s.

685

686 **Figure 3.** Frequency-wavenumber diagram calculated from ambient noise
687 cross-correlations. The white dashed line indicates the resolution limit (Gouédard et al.,
688 2008). Note that the power spectrum is normalized at each frequency.

689

690 **Figure 4.** Green's functions estimated for teleseismic P-waves: (a) radial and (b) vertical
691 components. The stations are sorted by their locations from WSW to ENE.

692

693 **Figure 5.** Joint inversion results for station HDA06. (a–c) Posterior probability of the (a)
694 number of layers, (b) standard deviation of the noise in phase velocity data, and (c)
695 standard deviation of the noise in Green's function data. (d–e) Input data (blue circles or
696 curve), distribution of model predictions (yellow–red heatmap), and the maximum a
697 posteriori (MAP) predictions (purple curves) for the (d) dispersion curve and (e) Green's
698 function. (f) Posterior marginal probability of the S-wave velocity as a function of depth.
699 The yellow–red heatmap indicates the probability; low probabilities (<0.01) are
700 transparently masked. The black line represents the reference velocity model. The green
701 line indicates the mode estimation (i.e., the maximum probability at each depth). The
702 purple line is the MAP estimation. Background colors discriminate the different
703 lithologies identified in this study.

704

705 **Figure 6.** Joint inversion results for all stations. Each panel shows the posterior marginal
706 probabilities of the S-wave velocity as a function of depth obtained for different stations.
707 The notations are the same as those in Figure 5f.

708

709 **Figure 7.** V_p/V_s estimations for all stations. The probability distribution of V_p/V_s is
710 calculated from V_s profile sampled by inversion and the reference V_p model, where the
711 former V_s profile is smoothed over depths with a running window of 1.5 km. Notations
712 are the same as Figure 6.

713

714 **Figure 8.** Lithology depths. (a) The depth of the top of the low-velocity zone (LVZ). The
715 station HDA01, whose velocity structure does not show an evident LVZ, is filled in black.
716 (b) Lithology top depths along the profile X–Y shown in (a). The square, triangle, circle,
717 and inverted triangle symbols denote the sedimentary units 2 (U2), 3 (U3), LVZ, and
718 deeper lithology, respectively. The black line represents the average seafloor depth across
719 the array. Error bars are 68% confidence intervals of the lithology depth. For HDA01, the
720 depth of LVZ top is not shown because of its absence in the results. (c) Teleseismic
721 Green's function at each station. The blue wiggles represent the observed stacked GFs.
722 The dotted purple lines are the predictions from the maximum a posteriori estimations.
723 The yellow–red heatmap represents the frequency distribution of the model predictions.
724 The green vertical bars indicate 68% confidence intervals of the arrival time of Ps
725 converted phases from the top of the LVZ. Again, the arrival time of HDA01 is not shown
726 due to the absence of the LVZ.

727

728 **Figure 9.** Fault traces from a compilation of seismic reflection surveys (Headquarters for
729 Earthquake Research Promotion, 2020). The sky-blue, green, and purple lines denote
730 thrust, strike-slip, and normal faults, respectively. The orange star denotes the location of
731 an array of ocean-bottom seismometers. The pink line denotes the subducted
732 Kyushu–Palau Ridge (Yamamoto et al., 2013).

733

734 **Figure 10.** Schematic illustration of possible causes of the low-velocity zone (LVZ) and
735 its depth offset. (a) A scenario by a blind fault. A blind fault induced by the subducted
736 Kyushu–Palau Ridge may act as fluid conduits to form the fluid reservoir. (b) Alternative
737 scenario by mud diapir. An overpressured mud diapir pierces into Unit 3.

738

Figure 1.

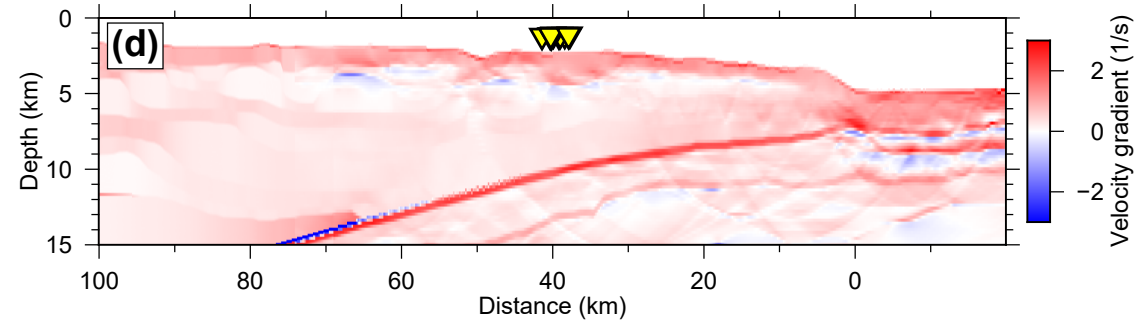
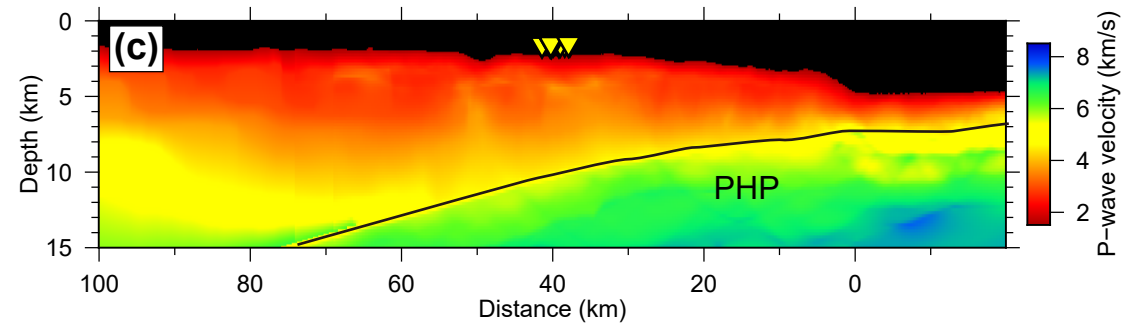
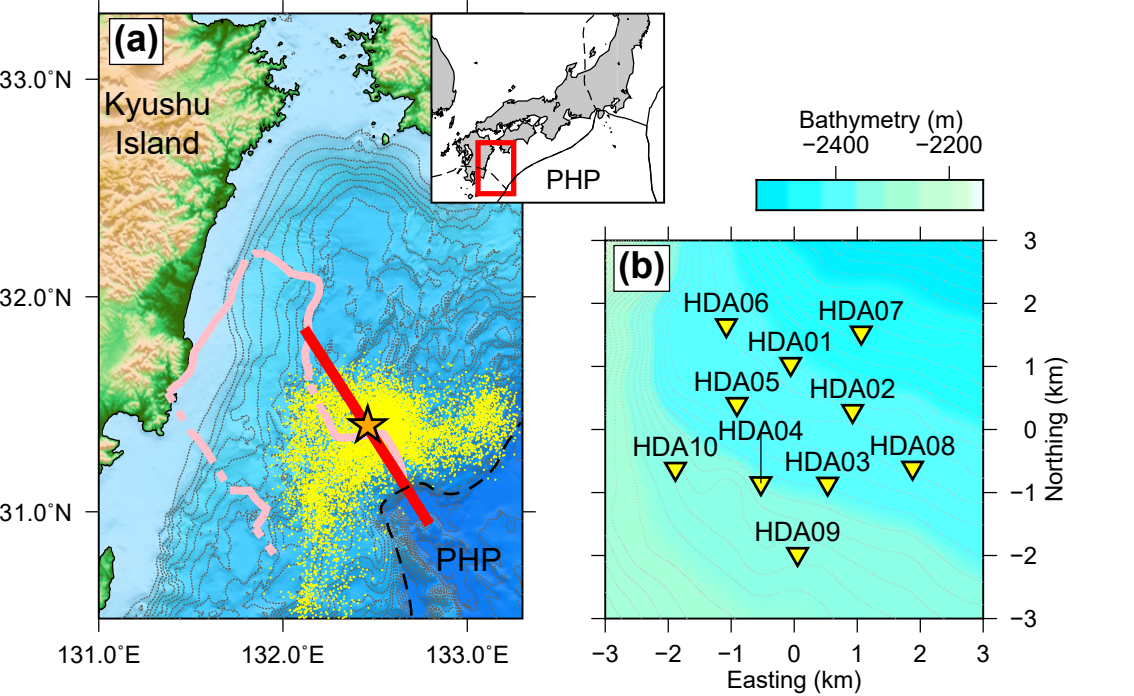


Figure 2.

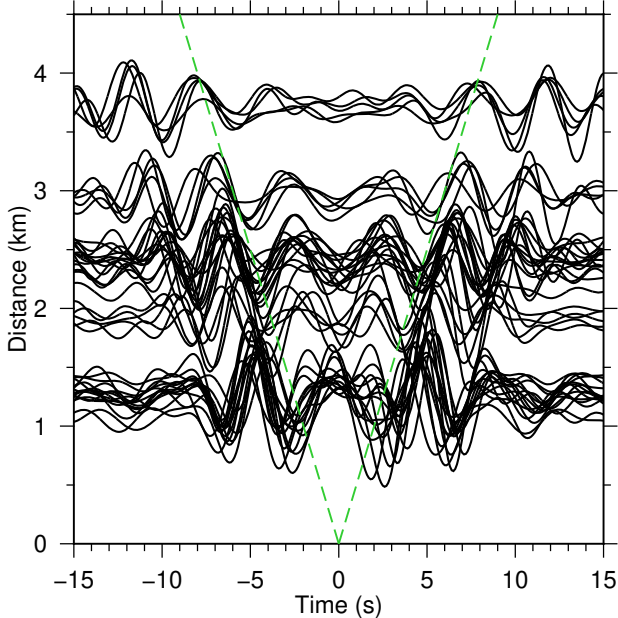


Figure 3.

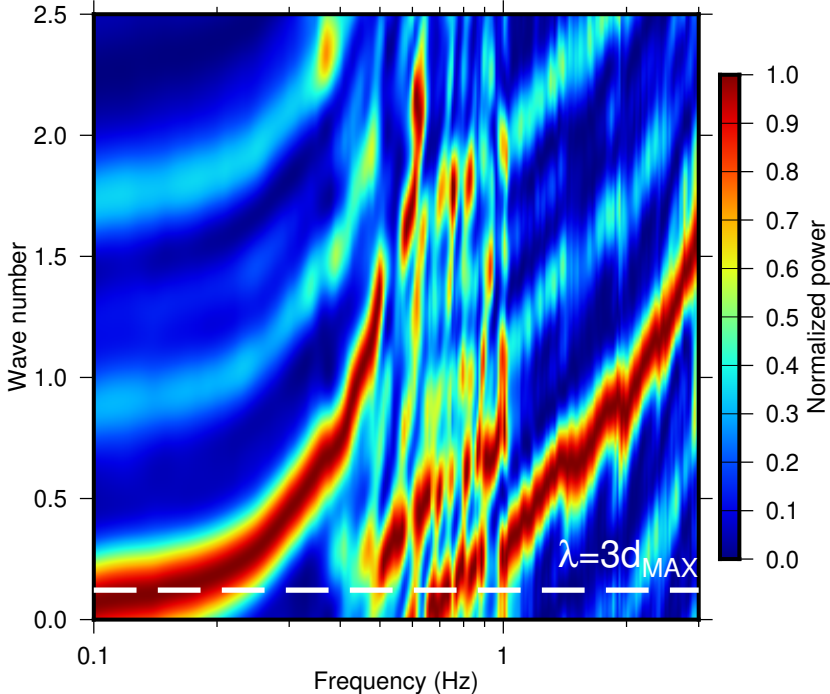


Figure 4.

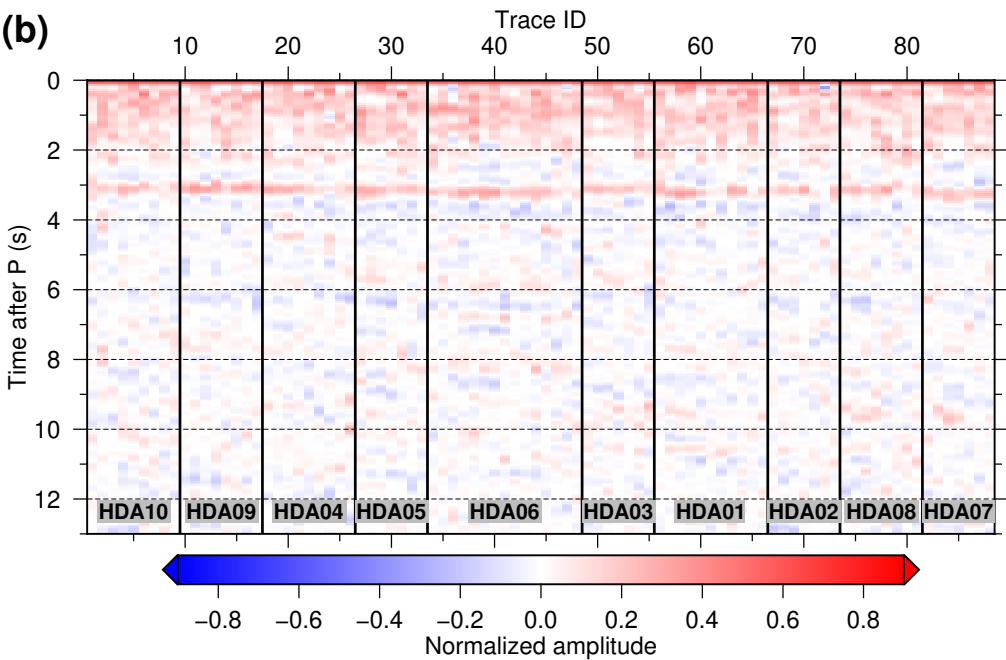
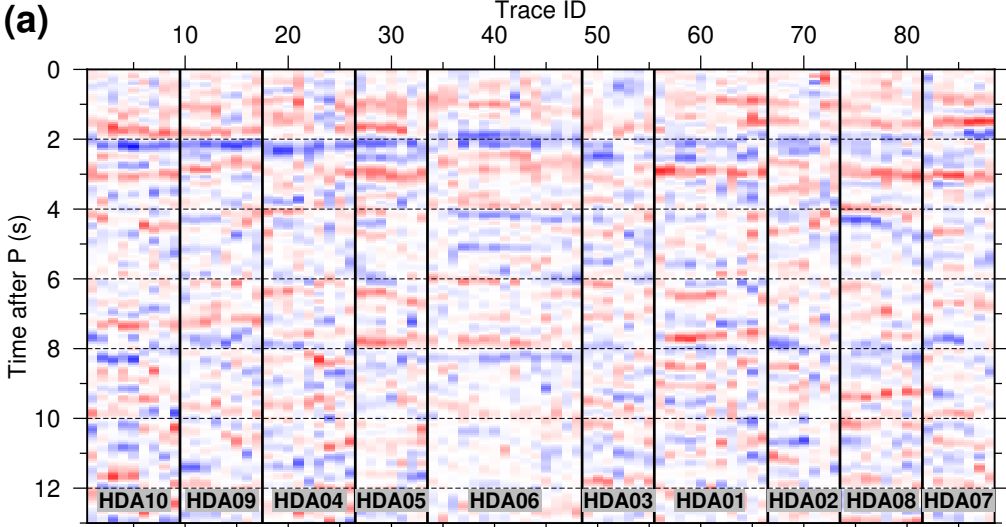


Figure 5.

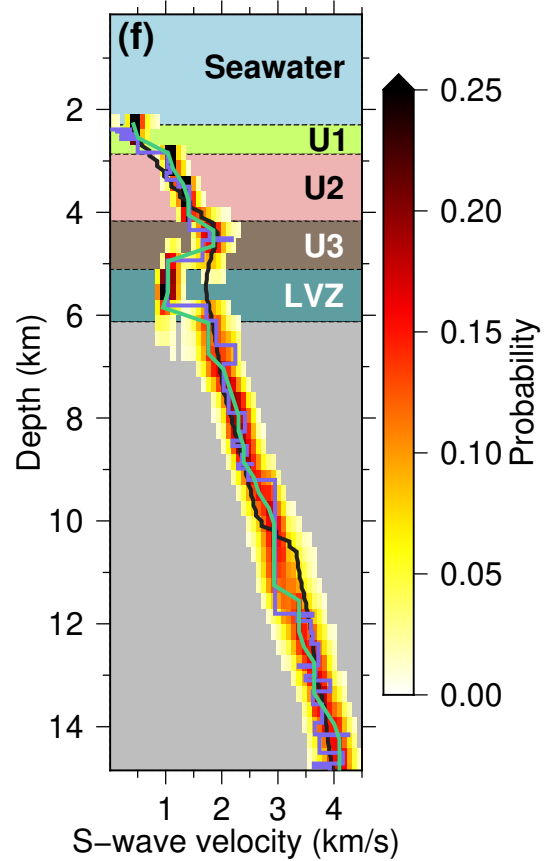
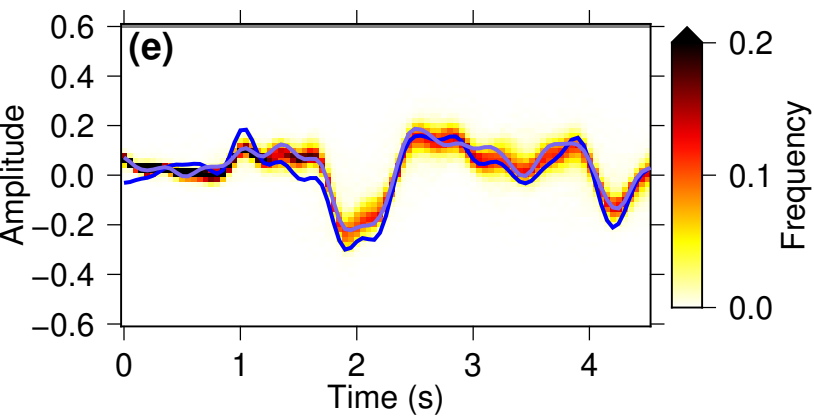
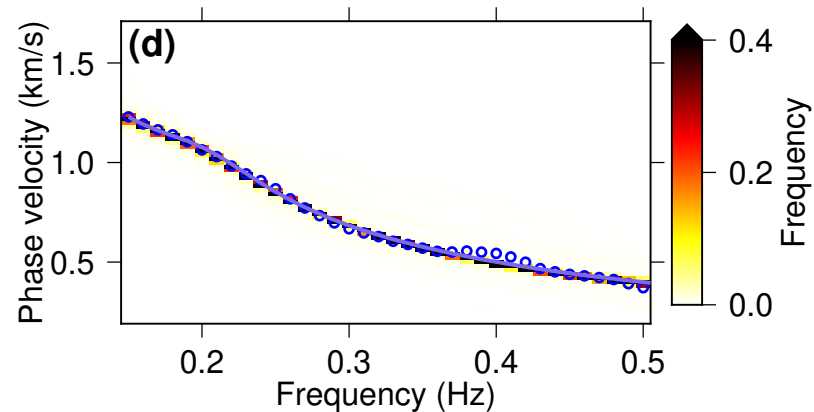
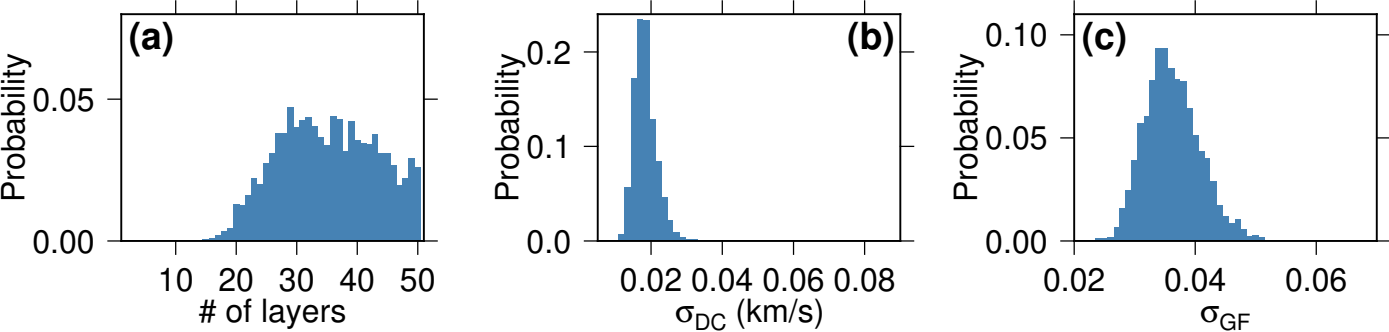


Figure 6.

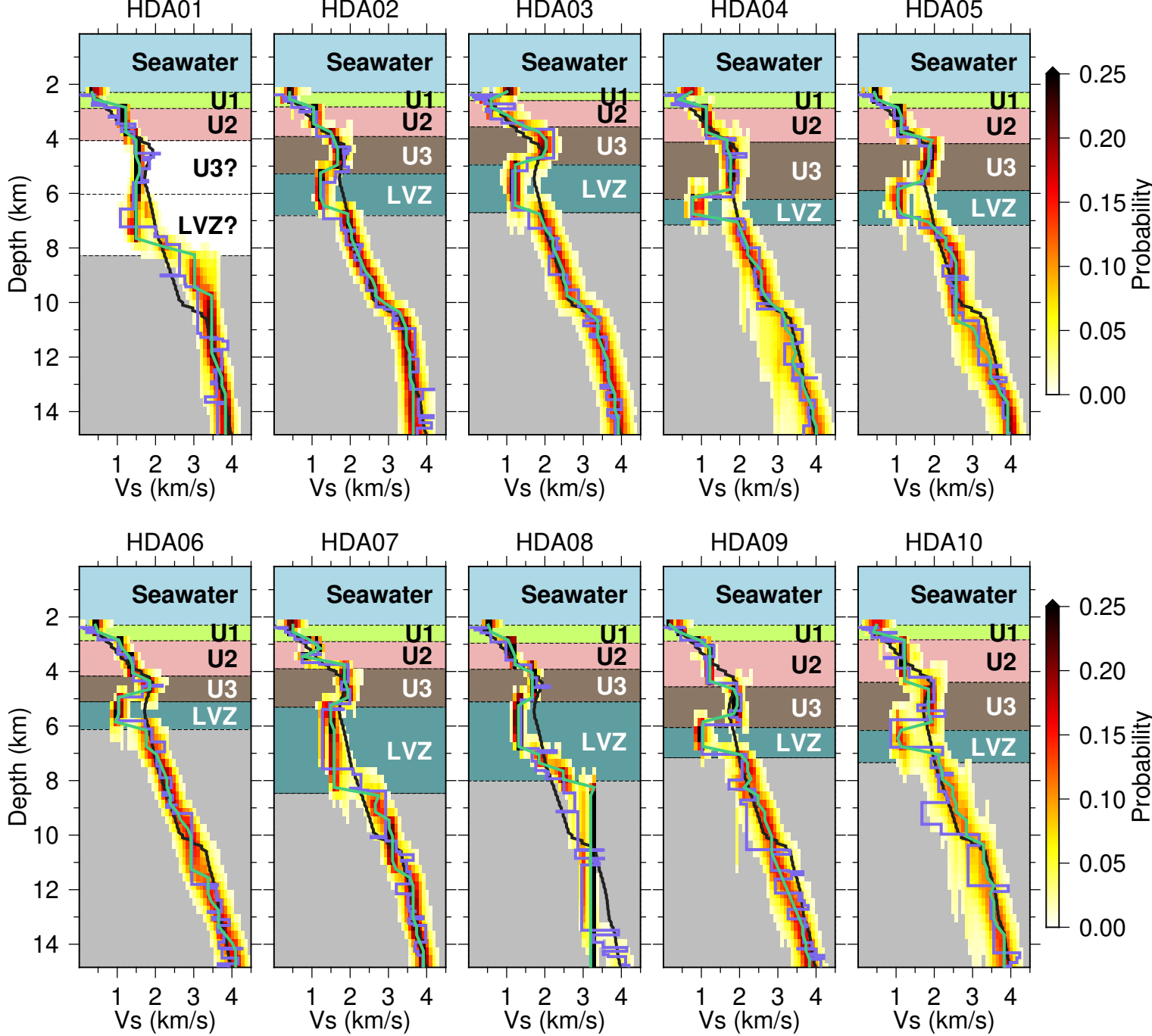


Figure 7.

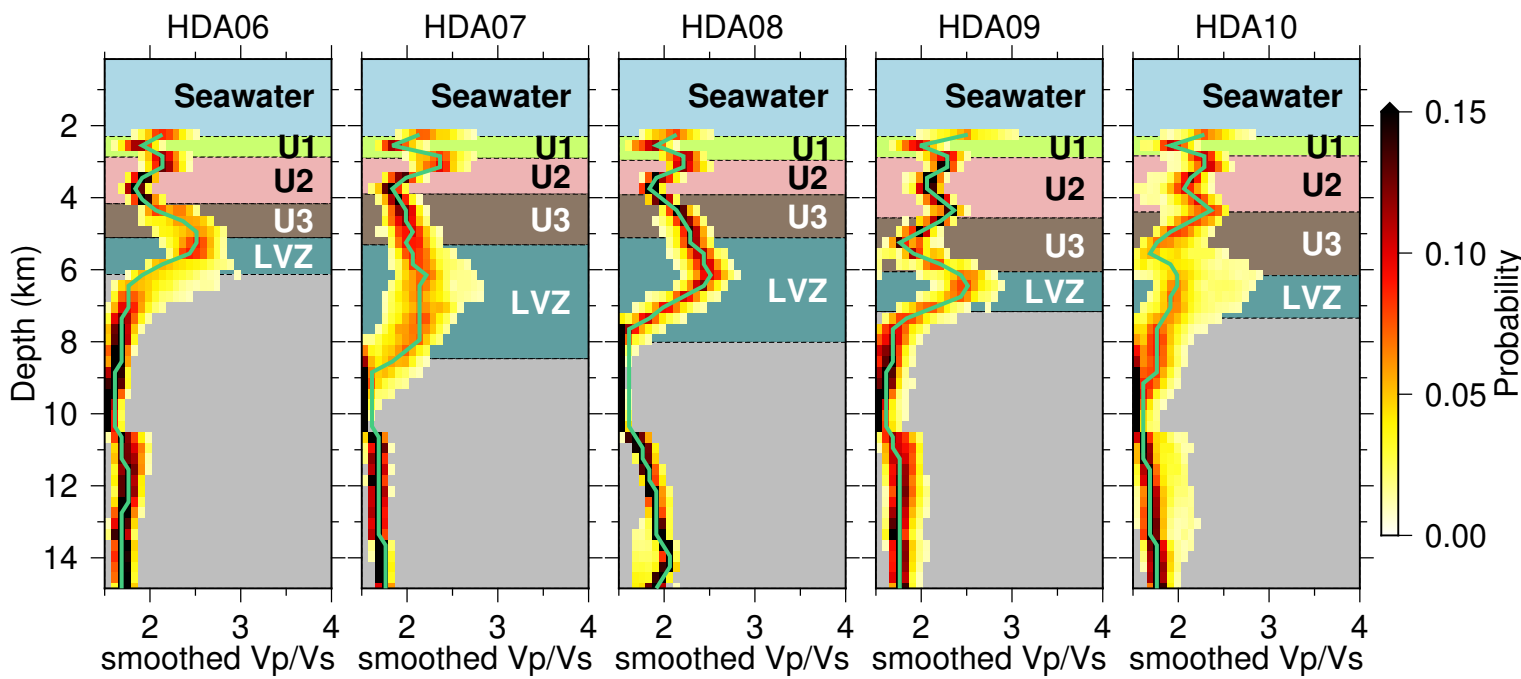
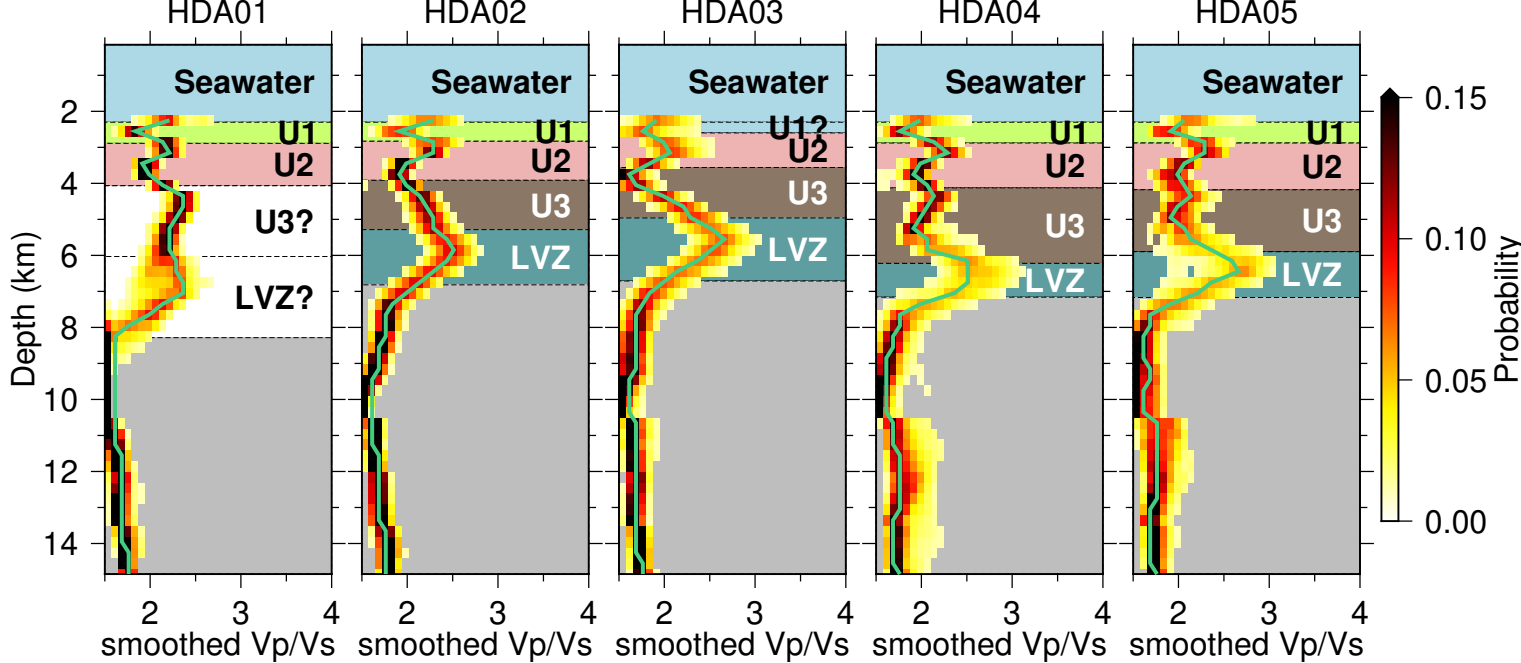


Figure 8.

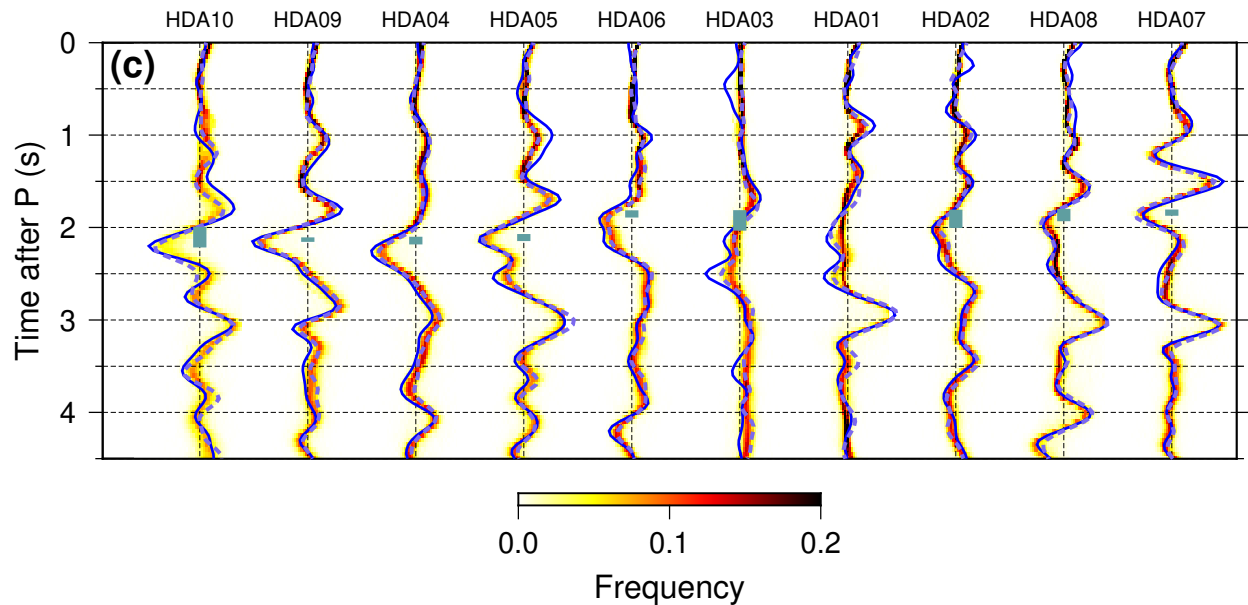
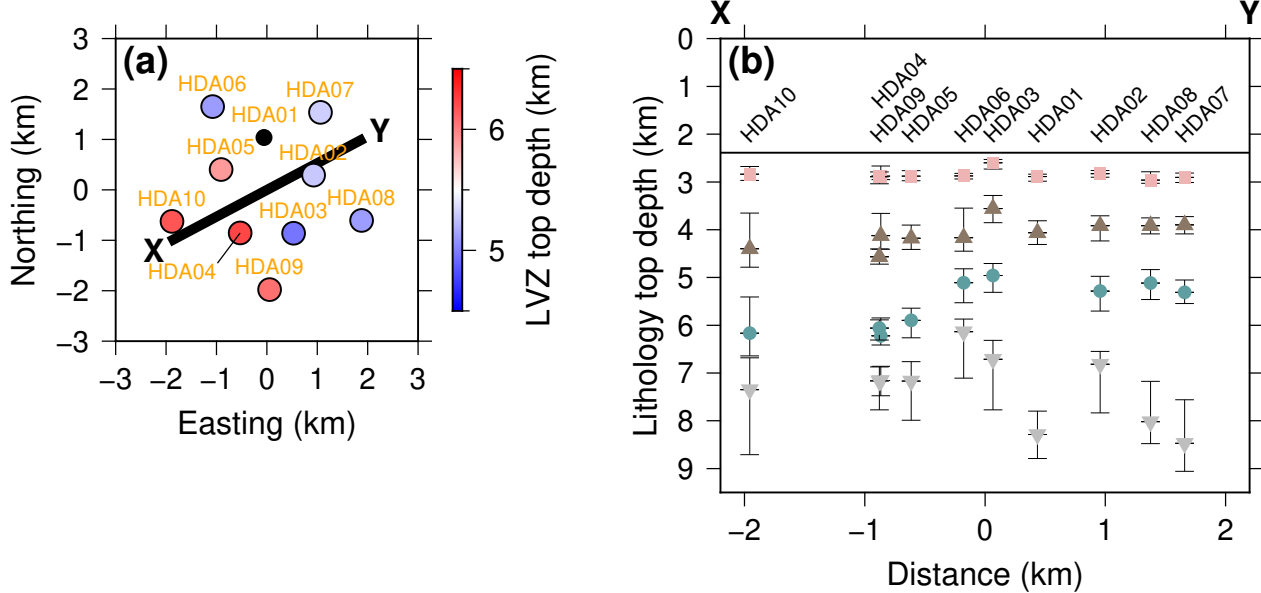


Figure 9.

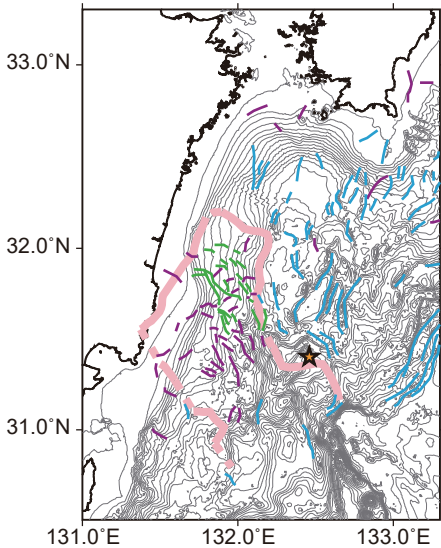
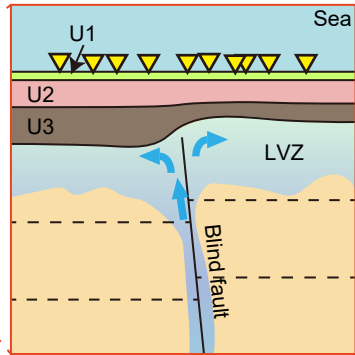
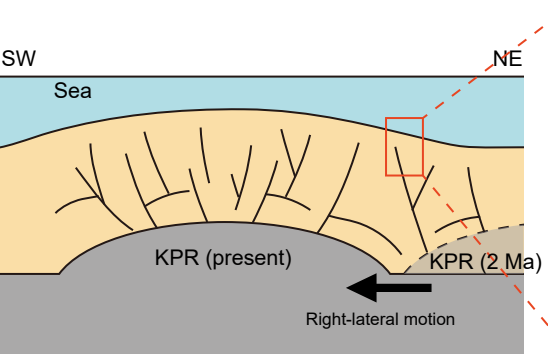


Figure 10.

(a)**(b)**